ESFD RESEARCH PROJECT NOVEMBER 22, 2026

Electromagnetic Spin–Field Dynamics

Master research paper and technical report

Christopher Grenke

Original research program

Spin and chirality, effective field theory, nonlinear stability, compact objects, gravity, and the cosmological and quantum extensions. Expanded archival synthesis with field derivations, rerun public datasets, and executable research benchmarks.

Contents

1 Research summary and scope 3

2 Spin from particles to rotating matter 5

3 Actions and field equations 8

4 A solved ESFD instability 12

5 Laboratory spin, phase, and inertia 16

6 Pulsars, magnetars, and flares 18

7 Neutron stars, mergers, and black holes 21

8 Gravity, geometry, and the spin–entropy proposal 23

9 Galaxies, the Great Attractor, and the dark sector 26

10 Spin–torsion collapse, white holes, and daughter universes 31

11 Quark and gluon spin, the Higgs field, and CERN 33

12 Exceptional symmetry and ultraviolet completion 35

13 Quantum coherence, collapse, and observers 36

14 Solar, geophysical, and vacuum extensions 37

15 Validation plan and decision criteria 39

16 Appendix A. Reconstruction ledger 42

17 Appendix B. Reproducible calculations and data dictionary 44

18 Sources and references 45

1 Research summary and scope

Electromagnetic Spin–Field Dynamics (ESFD) began with Christopher Grenke's question about why rotating systems lose stability and whether the local electromagnetic environment and the spins of their constituents can supply a common mechanism. The most expansive versions move from intrinsic spin and phase coherence through mass, inertia, and curvature to compact stars, cosmic structure, and the observer. A narrower formulation retains Einstein dynamics and asks where a measurable spin-dependent electromagnetic term changes the behavior of matter. This paper develops both formulations to the level permitted by the recovered equations and evidence. It preserves the early conjectures, specifies where a conjecture becomes a mathematical model, and evaluates the predictions that can be computed. A1 A2 A3 A4 A5 A6

Abstract. We reconstruct the June spin-tensor action, a later covariant exponential electromagnetic coupling, and the spin–entropy extension. The archived symbol χ denotes several dimensionally and operationally different quantities. Variational reconstruction distinguishes composite Dirac polarization from an independent collective field and gives a dimensionally closed independent-scalar example. In a quadratic scalar background, dynamical electromagnetic perturbations give a long-wavelength transverse instability above a specified field, with its own angular and finite-size conditions. Direct integration agrees with the predicted growth. This threshold follows from the new benchmark assumptions and involves an independently measurable product of field-theory scales. Its relation to stellar rotation requires a material response model. Archived catalog and observational tests were rerun from hashed snapshots. The timing-based $B\Omega$ index is exactly a transform of characteristic age and its historical cutoff selects 5 of 22 eligible ATNF AXP-tagged objects and 5 of 22 confirmed McGill magnetars with uncensored positive timing. An added projection cannot increase the passes at fixed field. The archived galaxy profile fits some data, with weaker performance on withheld outer radii than the tested NFW and pseudo-isothermal controls. A new magnetic-energy estimate quantifies the field needed if Maxwell energy supplies the inferred missing acceleration. Further development treats spin and chirality, quark and nucleon matching, gravitation and lensing, compact-object collapse, curved-space propagation, the Higgs and E_8 proposals, black-to-white-hole cosmology, and quantum and observer extensions as explicit research questions. The combined record yields falsified historical rules, reproducible reference results, and new conditional predictions for defined actions.

Research materials. The companion reproducibility archive includes source papers, the previous catalog pipeline and its raw input snapshots, the new spin calculations and figures, the editable manuscript, the historical claim register, and a branch-by-branch evidence index. This revision draws on 19 recovered originals, two related Pattern Nexus articles in local project working material, and identifiable excerpts from 2025–2026 project conversations. The archive logs 40 historical recovery leads, including original runs and file versions still unavailable. The reported GPT model versions of the earliest work are the author's recollection. Available file metadata dates versions and does not establish their model generation history. A1 A6 A8

Result	Evidentiary meaning
$B_{\text{tim}}\Omega/\Lambda_{\text{tim}} = \sqrt{1624.08\,\text{yr}/\tau_c}$	Algebraic identity with the adopted pulsar timing convention. The joint field and rotation interpretation requires a field estimate independent of the torque.
$B_c = \sqrt{2e}\, f_\Phi m_0/\lvert\xi\rvert$	Onset in the infinite homogeneous quadratic independent-scalar model for transverse waves. Finite size, angle, and medium response change the domain.
$p = 1.55 \times 10^{-4}$ at 10^{15} G	Population imbalance for the ideal zero-temperature neutron gas at $0.16\,\text{fm}^{-3}$. It is an explicit scale comparison for a proposed spin-alignment mechanism.
Median required $B_{\text{rms}} = 5.93 \times 10^4\,\mu$G	Magnetic-energy mass proxy from one outer point per fitted SPARC galaxy. The estimate tests ordinary Maxwell energy in a spherical weak-field approximation.
$a/a_b = [1 + (t/t_b)^2]^{1/3}$	Exact flat homogeneous toy bounce with dust and a negative stiff spin correction. The interior of a rotating black hole is a separate boundary-value problem.

1.1 The chronology and the hypotheses

The recovered June 3, 2025 manuscript sets out the two-form $S_{\mu\nu}$, the $B\Omega$ threshold, a saturation potential, and lab, merger, and heavy-ion tests. The adjacent chat synthesis and the later field draft introduce the exponential gauge-kinetic function and an Einstein–Cartan connection. A June quantum rewrite emphasizes the dipole operator. The spin–entropy and Electromagnetic Universe drafts introduce extra sources, and the July E_8 synthesis suggests a high-energy embedding. The later proof and re-evaluation papers include strong-field QED, energy accounting, compactness and rotational limits, torsion, and inertia. The 2026 CERN rewrite moves toward an off-shell spin-density observable. The subsequent observer work argues for a deeper organization of spacetime and measurement. These are dated version records and conceptual continuities. Chronology alone supplies no prospective prediction score. A1 A2 A3 A4 A5 A6

Three propositions organize this edition. **Spin response in an electromagnetic environment** is an operator and constitutive problem that can be interrogated in laboratory systems and stars. **A dynamical threshold or crossover** requires explicit unstable modes, competing timescales, or an energy landscape. **Emergence of gravity, time, or geometry** requires a derivation of an effective metric, its dynamics, and universal coupling from specified degrees of freedom. The three propositions carry distinct empirical burdens. A standard spin response or an ordinary electromagnetic instability establishes a baseline for testing the first two.

1.2 Conventions and the several quantities called chi

Use $c = \hbar = 1$ inside field-theory formulas, metric signature $(+ - - -)$, and Heaviside–Lorentz electromagnetic normalization $-\frac{1}{4}F^2$. Unit conversions and astronomical estimates state SI or Gaussian units explicitly. Write $M_{\rm P}^{-2} = 8\pi G$ for the reduced Planck scale. Let $F_{\mu\nu} = \partial_\mu A_\nu - \partial_\nu A_\mu$, $\tilde{F}^{\mu\nu} = \epsilon^{\mu\nu\rho\sigma}F_{\rho\sigma}/2$, $F^2 = 2(B^2 - E^2)$, and set the dual convention so $F\tilde{F} = -4\mathbf{E}\cdot\mathbf{B}$. The symbol Ω refers to a measured rotation rate or a vorticity specified by a model. For a timing period P, $\Omega = 2\pi/P$. One tesla equals 10^4 gauss. Threshold constants carry the units of their numerators.

Quantity	Definition and role
$\chi_{\rm tim}$	$B_{\rm tim}\Omega/\Lambda_{\rm tim}$, with $\Lambda_{\rm tim} = 6.28 \times 10^{14}$ G rad s^{-1}. Fixed June-draft astrophysical index.
χ_E	$(E_{\rm rot} + E_{\rm mag})/\lvert W\rvert$. Canonical energy comparison in *Testing*. Versions normalized by support energy use a different ratio.
b_e	B/B_Q, with $B_Q = m_e^2/e$ in natural units, 4.414×10^{13} G. Electron QED scale.
$\mathcal{C}$, a_*, $\chi_{\rm eff}$	$GM/(Rc^2)$, $cJ/(GM^2)$, and waveform mass-weighted aligned binary spins. Three relativistic quantities with different observables.
d_i or α	Low-energy species-dependent Pauli coefficient, mass dimension -1. The historical 10^{-3} label can parameterize a dimensionless moment convention after matching.
Φ, X	Dimensionless collective scalar and spin-bilinear invariant $X = S_{\mu\nu}S^{\mu\nu}$, with $[X] = 6$. A relation such as $\Phi = c_X X/M^6$ is an explicit model choice.
ξ, Λ_g	Slope of $Z(\Phi)$ and cosmological term in the historical gravitational action. They are independent of the timing normalization.

2 Spin from particles to rotating matter

2.1 Relativistic spin, polarization, and angular momentum

Wigner's massive one-particle spin label is specified by the Pauli–Lubanski vector $W^\mu = \frac{1}{2}\epsilon^{\mu\nu\rho\sigma}P_\nu J_{\rho\sigma}$ and $W^2 = -m^2 s(s+1)$ in these units. Quantum spin is a representation of rotations and Lorentz symmetry. A macroscopic rotor has angular momentum obtained from momentum density and any polarized constituent contribution. In flat space a decomposition reads

$$J^{ij} = \int d^3x\, [x^i T^{0j} - x^j T^{0i} + \mathcal{S}^{0ij}],$$

with a chosen stress and spin-current convention. Improvements of the stress tensor can move density between the orbital and spin pieces while preserving total charges under suitable boundary conditions. In a local rest frame a magnetic moment density can source a magnetization current, while bulk rotation can carry angular momentum in neutral, almost unpolarized matter. A galaxy's J, a Kerr remnant's a_*, a nucleon's spin, and a magnetar's polarized spin density accordingly require different measurement maps. R01 R04 R58

The recovered polarization tensor and the Dirac contribution to the spin current are related spinor constructions with different index structure:

$$S_{\mu\nu} = \tfrac{1}{2}\bar{\psi}\sigma_{\mu\nu}\psi, \qquad \sigma_{\mu\nu} = \tfrac{i}{2}[\gamma_\mu, \gamma_\nu], \qquad \mathcal{S}^{\lambda\mu\nu} = \tfrac{1}{4}\bar{\psi}\{\gamma^\lambda, \sigma^{\mu\nu}\}\psi.$$

The antisymmetrized Dirac spin current is dual to an axial current $J_5^\mu = \bar{\psi}\gamma^\mu\gamma^5\psi$ up to conventions. A torsion equation sourced by $\mathcal{S}^{\lambda\mu\nu}$ needs a tetrad and spin connection. A constitutive equation involving $S_{\mu\nu}$ instead models polarization or tensor order. With ε_S and $\mathbf{s}_S$ conventions analogous to the electric and magnetic parts of F, $X = 2(|\mathbf{s}_S|^2 - |\boldsymbol{\varepsilon}_S|^2)$. Thus $\sqrt{X}$ as printed in one manuscript requires a magnetic-type sector, $X \geq 0$, or a specified alternative norm. A potential minimized at $X = \Phi_0^2$ can model a preferred tensor invariant. Its minimum alone gives neither a hard upper bound on amplitudes nor a stable Hamiltonian for a general dynamical tensor. A1 R01

For a medium with four-velocity u^μ, define $B^\mu = \tilde{F}^{\mu\nu}u_\nu$, $E^\mu = F^{\mu\nu}u_\nu$, and the vorticity vector $\omega^\mu = \frac{1}{2}\epsilon^{\mu\nu\rho\sigma}u_\nu\nabla_\rho u_\sigma$. The positive field magnitude is $\sqrt{-B_\mu B^\mu}$. A covariant candidate for a rotation–field projection is $-B_\mu\omega^\mu$. In a rigid, slowly rotating local patch it reduces to $\mathbf{B}\cdot\boldsymbol{\Omega}$ when $\frac{1}{2}\nabla\times\mathbf{v} = \boldsymbol{\Omega}$. A spin dipole can also couple to B^μ in a medium at rest. A zero bulk vorticity therefore leaves spin magnetization possible. The action rather than the timing index determines vacuum decoupling.

2.2 Direction, chirality, and field helicity

Helicity is angular momentum projected on the direction of momentum. Chirality projects relativistic fields with $P_{L,R} = (1 \mp \gamma^5)/2$. For massless free fermions, particle helicity tracks chirality with the conventional particle/antiparticle assignments. A massive fermion can be observed from a frame where its momentum direction reverses. A reversal of rotor direction, a flip of a magnetic field, and a reversal of microscopic spin polarization implement different operations. $\mathbf{B}$ and $\boldsymbol{\Omega}$ are axial vectors, so $\mathbf{B}\cdot\boldsymbol{\Omega}$ is parity even and time-reversal even under simultaneous reversal. $\mathbf{E}\cdot\mathbf{B}$ is parity odd and time-reversal odd. Operators with $\tilde{F}$, pseudoscalars, and handed backgrounds can therefore be tested through parity-specific signatures rather than collected under a generic spin label. R03 R30

Magnetic helicity $K_B = \int_V \mathbf{A}\cdot\mathbf{B}\,d^3x$ quantifies field linkage for a closed boundary with $\mathbf{B}\cdot\hat{\mathbf{n}} = 0$. Its time evolution is $dK_B/dt = -2\int_V \mathbf{E}\cdot\mathbf{B}\,d^3x$ plus surface flux. Open solar and astrophysical volumes require relative helicity with an appropriate reference field. Fluid helicity $\int \mathbf{v}\cdot(\nabla\times\mathbf{v})\,dV$ is a different scalar under rotations and pseudoscalar under parity. Ideal MHD conserves magnetic topology under appropriate flux constraints, while reconnection and boundary flows can change connectivity. A rotating magnetosphere can possess structured helicity when the spatial average of the fermion tensor spin is small. Comparing a candidate ESFD onset with current-sheet formation and helicity injection isolates a physically distinct test.

A chiral magnetic current in a model with nonzero axial chemical potential has the response $\mathbf{j}_{\mathrm{CME}} = N_c\sum_f q_f^2\mu_5\mathbf{B}/(2\pi^2)$ in the standard homogeneous constitutive idealization. The finite lifetime of the collision field, charge conservation, axial relaxation, equilibrium boundary conditions,

and hadronization are essential in applying it. The axial anomaly connects $F\tilde{F}$ and the gluonic topological density with the divergence of J_5^μ, alongside fermion masses. It gives a baseline mechanism for handed charge separation. It supplies neither a conversion of quark spin to an object's classical Ω nor a normalization for the historical universal cutoff. R17 R18 R30

2.3 From microscopic correlations to field order

Consider N independent spin-$\frac{1}{2}$ projections along one direction, $s_i = \pm 1$, with $\langle s_i \rangle = p$. Their mean-square average is

$$\left\langle \left(\frac{1}{N} \sum_i s_i \right)^2 \right\rangle = \frac{1}{N} + \left(1 - \frac{1}{N}\right) p^2.$$

For interacting spins the right hand side acquires $N^{-2} \sum_{i \neq j} \mathrm{Cov}(s_i, s_j)$. This is the microscopic place to put coherence or a polarization correlation length. A macroscopic mean is order Np. Zero mean can coexist with order-N total variance. Long-range order changes the scaling, and a fluid or galaxy model must specify whether its effective field sees a mean, a renormalized local composite, or a spatially integrated correlation. In particular $\langle S_{\mu\nu} S^{\mu\nu} \rangle$ and $\langle S_{\mu\nu} \rangle \langle S^{\mu\nu} \rangle$ are different expectation values. Their separation matters for both the proposed halo and the Einstein–Cartan fluid.

A useful control is a free spin doublet with magnetic energy $-\mu B s$, giving $p_{\mathrm{th}} = \tanh(\mu B / k_B T)$. Independent electrons at 4 T and 4 K yield $p_{\mathrm{th}} = 0.586$ in this simple limit. At 10 μG and 8000 K the same expression gives 8.40×10^{-14}. Conducting, ordered, and degenerate matter need an appropriate susceptibility. For cold free neutrons of total number density n, spin populations $n_\pm = n(1 \pm p)/2$ give nonrelativistic Fermi energies $E_{F,\pm} = E_F (1 \pm p)^{2/3}$ with $E_F = \hbar^2 (3\pi^2 n)^{2/3} / (2 m_n)$. Equating chemical potentials including Zeeman energy yields

$$(1+p)^{2/3} - (1-p)^{2/3} = \frac{2|\mu_n| B}{E_F}, \qquad p \simeq \frac{3|\mu_n| B}{2 E_F}.$$

At $n = 0.16\,\mathrm{fm}^{-3}$ the illustrative E_F is 58.45 MeV. The population imbalance is 1.55×10^{-4} at 10^{15} G and 0.0155 at 10^{17} G. The independent-spin thermal expression at 10^8 K yields 0.604 at the first field. The zero-temperature free model reaches full polarization around 7.69×10^{18} G. Near that scale magnetic stresses and interaction, composition, relativistic, and superconducting corrections require a realistic equation of state. For the same ideal gas $M = n|\mu_n|p$, and the SI weak-field differential susceptibility gives $\mu_0\, dM/dB = 3\mu_0 n \mu_n^2 / (2E_F) \simeq 3.0 \times 10^{-3}$. This scale can anchor a weak-field closure before strong interactions and composition corrections. The calculation shows how a naive use of thermal alignment can inflate a candidate gravitational or electromagnetic source. It is a new controlled benchmark using physical constants and an assumed density.

2.4 Spin dynamics and electromagnetic dominance by regime

A minimal local closure in matter uses a magnetization response tensor $\delta M_i(\omega, \mathbf{k}) = \mathcal{X}_{ij}(\omega, \mathbf{k}) \delta B_j + \mathcal{Y}_{ij} \delta \omega_j$ with a stated equilibrium, constituent densities, and relaxation times. One rest-frame model adds $\dot{\mathbf{M}} = \gamma \mathbf{M} \times \mathbf{B} - (\mathbf{M} - \mathbf{M}_{\mathrm{eq}})/T_1$ for a single relaxation scale. Distinct longitudinal/transverse relaxation, spin transport, and backreaction enter realistic calculations. For a passive equilibrium

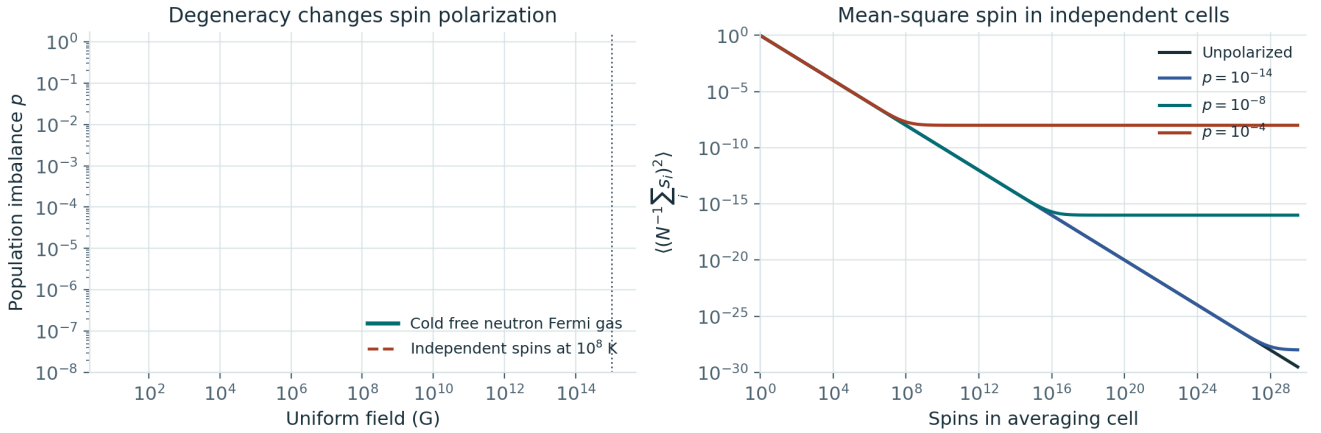


Figure 1. Spin polarization and coarse graining. Left, independent thermal neutron spins at an assumed temperature and a zero-temperature free gas at nuclear density. Right, the mean-square signed projection for independent spins at prescribed average polarization. Both are theoretical controls for the ESFD spin source.

the absorptive and dispersive parts of a causal susceptibility are related through Kramers–Kronig. An instability corresponds to a pole in the appropriate response or a negative second variation with dynamical constraints specified. Merely increasing a parameter that multiplies a current fails to define where a mode grows.

A separate comparison uses the magnetization parameter $\sigma_{\mathrm{MHD}} = B_{\mathrm{com}}^2/(\mu_0 w)$, where w is enthalpy density including rest energy, and the plasma beta $\beta_{\mathrm{pl}} = 2\mu_0 p_{\mathrm{gas}}/B_{\mathrm{com}}^2$. A tenuous magnetosphere may have $\sigma_{\mathrm{MHD}} \gg 1$ and be electromagnetically dominated in its plasma dynamics. An electrically neutral galaxy can have a dynamically important organized field in its gas, while total gravity determines stellar orbits and lensing. The two statements use different equations and energy inventories. A field that controls flows can be far too weak in mass-equivalent energy to account for measured gravitational potentials. Electromagnetic and gravitational forces between individual charged particles give a poor measure of collective charge neutrality, field stress, or universal coupling. R05 R08 R26

3 Actions and field equations

3.1 The June Dirac–Pauli version

With $\mathfrak{S}$ for the action and a historical cosmological constant label, the June manuscript gives

$$\mathfrak{S}_{6\text{–}3} = \int d^4x\sqrt{-g}\Big[\frac{R-2\Lambda_{\mathrm{cc}}}{16\pi G} + \bar{\psi}(i\gamma^\mu D_\mu - m)\psi - \frac{1}{4}F_{\mu\nu}F^{\mu\nu} + \alpha S_{\mu\nu}F^{\mu\nu} - \frac{\lambda_S}{4}\big(X-\Phi_0^2\big)^2\Big]. \tag{1}$$

Here $[A] = 1$, $[F] = 2$, $[\psi] = 3/2$, $[S] = 3$, $[\alpha] = -1$, $[\Phi_0] = 3$, and $[\lambda_S] = -8$ as mass dimensions. Expanding the potential gives a vacuum term, a dimension-six four-fermion interaction, and a dimension-twelve eight-fermion interaction. The vacuum term is part of the vacuum-energy matching. A nonzero minimum at positive X could break Lorentz symmetry in a specified state.

The potential sets the energetics of the invariant, and the constitutive map to a macroscopic $B\Omega$ must still be supplied. A1 A2

For the variation fix the current convention by $D_\mu = \nabla_\mu + iqA_\mu$, so minimal coupling contributes $-J^\mu A_\mu$ and $J^\mu = q\bar{\psi}\gamma^\mu\psi$. At fixed tetrad and spin connection, with the standard Hermitian Dirac kinetic term understood, variation gives

$$\begin{aligned} \nabla_\mu H^{\mu\nu} = J^\nu, \qquad H^{\mu\nu} = F^{\mu\nu} - 2\alpha S^{\mu\nu}, \\ 0 = \left[i\gamma^\mu D_\mu - m + \frac{\alpha}{2}\sigma_{\mu\nu}F^{\mu\nu} - \frac{\lambda_S}{2}(X - \Phi_0^2)S^{\mu\nu}\sigma_{\mu\nu} \right] \psi. \end{aligned} \tag{2}$$

The factors follow from $\delta_{\bar{\psi}} X = S^{\mu\nu}\delta\bar{\psi}\,\sigma_{\mu\nu}\psi$ and $\delta F_{\mu\nu} = 2\partial_{[\mu}\delta A_{\nu]}$. The Hermitian Dirac form also fixes how the connection and volume element vary in a torsion treatment. Gauge invariance gives $\partial_\nu(\sqrt{-g}J^\nu) = 0$ from the antisymmetric excitation, with $dF = 0$. In torsion spacetime use the exterior derivative for F, and express the Maxwell equation as a density divergence or as an exterior form. Using a torsionful covariant curl without torsion compensation changes the gauge transformation. Ordinary QED includes a spin magnetic moment even at zero bulk rotation. α represents an additional matched dipole in a physical application. R01 R02

The pure Pauli vertex has a transverse photon insertion, schematically $\delta\Gamma^\nu \propto \sigma^{\nu\mu}q_\mu$, with $q_\nu\delta\Gamma^\nu = 0$. A prescribed constant S makes the interaction linear in F a boundary term in free Maxwell variation. Changes in wave dispersion then require a dynamical spin response, nonuniform backgrounds, or other quadratic terms. A self-energy linear in a constant, antisymmetric $S^{\mu\nu}$ by itself supplies no consistent photon mass. Gauge-invariant media can have dispersive collective modes, and a longitudinal massive mode requires its own mechanism. The 10^{-9}–10^{-8} eV and 10–100 GeV scales associated in the June draft differ by about 10^{18}–10^{20} in energy, depending on endpoints. Photon splitting and pair creation require separate QED kinematics involving the background and polarization. A1 R06

3.2 The recovered covariant exponential action

The June 3 synthesis and later recaps use a different electromagnetic sector. With the connection written explicitly, the recovered form is

$$\begin{aligned} \mathfrak{S}_{\text{exp}} = \int d^4x\sqrt{-g}[\frac{R(\Gamma) - 2\Lambda_g}{16\pi G} - \frac{1}{4}e^{-\xi\Phi_{\text{EM}}}F_{\mu\nu}F^{\mu\nu} \\ + \frac{1}{2}\partial_\mu\Phi_{\text{EM}}\partial^\mu\Phi_{\text{EM}} - V(\Phi_{\text{EM}}) + \mathcal{L}_{\text{matter}}(\psi, D\psi; g, \Gamma)]. \end{aligned} \tag{3}$$

One historical potential uses a quadratic plus quartic, with positive quadratic curvature for a massive excitation. The historical discussion gives $\Phi_{\text{EM}} = \kappa_{\text{EM}}^2 X$ and also uses $\kappa_{\text{EM}} = 1/\Lambda_{\text{tim}}$ when normalizing $B\Omega$. In natural units $B\Omega$ and a Dirac bilinear each have dimension three. The numerical matching between the bulk product and the local operator needs material physics and a chosen conversion. A historical variant gives $\Phi_{\text{EM}} \propto S_{\mu\nu}F^{\mu\nu}$ instead. An exponent requires a dimensionless product. With $[\Phi] = 0$, $[\xi] = 0$ and a coefficient f_Φ^2 in front of the kinetic term supplies its required mass dimension. Three consistent implementations follow. They have different propagating variables and tests. A6

3.2.1 Independent dimensionless scalar

Take $Z = e^{-\xi\Phi} > 0$, $f_\Phi > 0$, and $\mathcal{L}_\Phi = f_\Phi^2(\partial\Phi)^2/2 - V(\Phi)$, with $[V] = 4$. In the minimally specified model,

$$\begin{aligned} \nabla_\mu(ZF^{\mu\nu}) &= J^\nu, \\ f_\Phi^2\Box\Phi + V'(\Phi) &= -\frac{1}{4}Z'(\Phi)F^2 = \frac{\xi}{4}ZF^2. \end{aligned} \tag{4}$$

A separately declared matter coupling $+\Phi c_X X/M^2$ adds $+c_X X/M^2$ on the right of the scalar equation. It also changes the matter equation. The spin source in this version is an extra operator. The archival variation simultaneously used a function of the spinor and a freely varied scalar. Equation (4) is the independent-field result with the matter dependence spelled out. A new spin closure must tie the local field to spin density or spin correlations to make the independent scalar specifically predictive of rotation.

3.2.2 Composite scalar built from spin

Set $\Phi = C(X) = c_X X/M^6$ before varying. Then $Z(C)$ multiplies the photon kinetic term. Its leading mixed operator is $+\xi c_X XF^2/(4M^6)$. If the composite kinetic term is retained it becomes $f_\Phi^2(\partial C)^2/2$, a derivative interaction of the spinor. Assuming no explicit F in C, the scalar-sector contribution to the Dirac variation is $\mathcal{E}_C\, C'(X)S^{\mu\nu}\sigma_{\mu\nu}\psi$, where

$$\mathcal{E}_C = -f_\Phi^2\Box C - V'(C) - \frac{1}{4}Z'(C)F^2. \tag{5}$$

$\mathcal{E}_C$ is a variation factor and becomes an independent field equation only in the independent branch. In the constrained formulation add $+\ell(\Phi - C)$, where ℓ is a multiplier of mass dimension four. The ℓ equation ensures $\Phi = C$, the Φ equation sets $\ell = -\mathcal{E}_C$, and the $\bar\psi$ equation then reproduces (5). Derivative composite interactions are used perturbatively within their cutoff unless a controlled extra-mode analysis is supplied.

If instead $C = c_{SF}S_{\mu\nu}F^{\mu\nu}/M^5$, C depends directly on F. With the derivative term included, the excitation is $H^{\mu\nu} = ZF^{\mu\nu} - 2\mathcal{E}_C\,\partial C/\partial F_{\mu\nu}$, up to any separate Pauli term. This expression uses the Euler derivative of the full scalar sector and integrates by parts before varying F. In the algebraic limit it includes the Z' and V' contributions to the excitation. Treating this model as a background scalar Maxwell dielectric would omit the implicit-field terms. Its higher variations and symmetries require a distinct audit. A6

3.2.3 Independent two-form and spin transport

A classical tensor can instead be given healthy auxiliary dynamics as a massive antisymmetric two-form $Q_{\mu\nu}$ of mass dimension one. A test completion on torsionless spacetime uses $K = dQ$ and

$$\begin{aligned} \mathcal{L}_Q &= \frac{1}{12}K_{\mu\nu\rho}K^{\mu\nu\rho} - \frac{m_Q^2}{4}Q_{\mu\nu}Q^{\mu\nu} + \frac{g_Q}{2}Q_{\mu\nu}F^{\mu\nu}, \\ \nabla_\rho K^{\rho\mu\nu} + m_Q^2 Q^{\mu\nu} &= g_Q F^{\mu\nu}. \end{aligned} \tag{6}$$

For $m_Q > 0$, the massive two-form has three spin-one degrees of freedom in four dimensions. The leading long-wavelength elimination gives $Q \simeq g_Q F/m_Q^2$ and $Z_{\text{eff}} = 1 - g_Q^2/m_Q^2$, which must be positive for a healthy photon kinetic term. For this quadratic model the shift $Q \mapsto Q - g_Q F/m_Q^2$ preserves K by $dF = 0$ and diagonalizes the action locally. An observable needs additional stated response terms, for example a $Q_{\mu\nu}S^{\mu\nu}$ coupling and matched boundary conditions. The unqualified $D^2S + \partial V/\partial S = \chi F$ in the E_8 working notes leaves open the kinetic sign, constraints, and relation to the fermion bilinear. Equation (6) illustrates a way to address these requirements. A6

3.3 Stress, curvature, and connection response

In the torsionless benchmark define $T_{\mu\nu} = 2\delta\mathfrak{S}_m/(\sqrt{-g}\delta g^{\mu\nu})$. Write $G_{00}^{\text{geom}} = 3H^2$ in flat FLRW. With the positive stress variation for signature $(+---)$, take $R_{\text{archive}} = -R_{\text{geom}}$ in the positive Einstein–Hilbert term of (1) and (3). The result is $G_{\mu\nu}^{\text{geom}} - \Lambda_g g_{\mu\nu} = 8\pi G\, T_{\mu\nu}$ in (3), and the corresponding equation with Λ_{cc} in (1). Equivalently absorb the cosmological term into a vacuum stress. For independent Φ the two stress contributions are

$$\begin{aligned} T_{\mu\nu}^F &= Z\left[-F_{\mu\alpha}F_{\nu}{}^{\alpha} + \frac{1}{4}g_{\mu\nu}F^2\right], \\ T_{\mu\nu}^{\Phi} &= f_\Phi^2\partial_\mu\Phi\partial_\nu\Phi - g_{\mu\nu}\left[\frac{1}{2}f_\Phi^2(\partial\Phi)^2 - V(\Phi)\right]. \end{aligned} \tag{7}$$

Vary a spinor action with respect to the tetrad to include the spin matrices, the volume term, and its spin connection. A composite C gives additional implicit metric or tetrad variations. In a self-consistent solution the gradients of Z exchange energy and momentum between electromagnetic and scalar sectors, and the combined stress with matter is covariantly conserved. For GR plus matter the stress is the gravitational source and the coupling G is already present in the action. Deriving G from a new microscopic model remains a distinct task.

For minimal Einstein–Cartan gravity, start with $(e_\mu{}^a, \omega_\mu{}^{ab})$ independent and vary a metric-compatible spin connection. Torsion is algebraic, proportional to the Dirac axial spin current with coefficient of order G. Eliminating it generates an axial four-fermion contact term of order $M_{\text{P}}^{-2}J_5 \cdot J_5$. An explicit convention, the spin ensemble, and the averaging order are required for its sign and effective pressure. This interaction is short-range in the minimal theory. A propagating torsion extension must state its kinetic action, mode spectrum, and couplings. Laboratory search bounds then depend on range and spin structure. R01 R27

3.4 Effective field theory, quantization, and matching

The operator $S_{\mu\nu}F^{\mu\nu}$ is dimension five below electroweak breaking. In the moment convention $\mathcal{L} \supset (q\,\delta a/4m)\bar{\psi}\sigma^{\mu\nu}\psi F_{\mu\nu}$, an additive Pauli coefficient implies $\delta a = 2m\alpha/q$. Its sign follows the chosen charge convention. The QED contribution $a = (g-2)/2 = \alpha_{\text{em}}/(2\pi) + \cdots$ is already included in Standard Model matching. A new electron residual is tested using the independently inferred fine-structure constant and its error. One can translate a conditional uncertainty ϵ_a into $|\alpha| \lesssim |q|\epsilon_a/(2m)$ in a one-operator fit. The old statement that the same $\chi \sim 10^{-3}$ describes a measured moment, a Lagrangian coefficient, and a torque threshold mixes observables and dimensions. Nucleons carry composite magnetic moments and tensor matrix elements. Their coefficients require hadronic matching instead of the electron formula alone. A2 A6 R02

Above electroweak breaking chirality and gauge charges govern the operator basis. For example $\bar{Q}_L \sigma^{\mu\nu} u_R \tilde{H} B^Y_{\mu\nu}$ and $\bar{Q}_L \sigma^{\mu\nu} T^A u_R \tilde{H} G^A_{\mu\nu}$ are dimension-six electroweak-gauge-invariant dipoles, with Hermitian conjugates and appropriate flavor coefficients. Both chiralities enter a dipole even though $\sigma^{\mu\nu}$ commutes with γ^5, since $\bar{\psi}_L = \bar{\psi} P_R$. Below the Higgs vacuum expectation value, the hypercharge and weak dipoles give photon and Z dipoles and the chromomagnetic dipole gives a separate strong-sector interaction. Electroweak quantum numbers, scale running, hadronic tensor charges, and experimental observables enter the matching. The spin–electromagnetic XF^2 composite is dimension ten. A quark operator $(D_\rho S^q_{\mu\nu})^2$ is dimension eight, with corresponding scale suppression. Keeping the Standard Model gauge symmetries and anomaly-free matter content preserves the usual anomaly cancellations within the effective description. New chiral matter or gauge groups require their own analysis. R03

A concrete matching calculation in the independent branch expands $\Phi = s/f_\Phi$ about zero and $Z = 1 - \xi s/f_\Phi + \cdots$. At energies and momenta well below the scalar mass m_0, the leading tree correction from integrating out s is

$$\Delta\mathcal{L} = \frac{\xi^2}{32 f_\Phi^2 m_0^2} (F^2)^2. \tag{8}$$

This follows by solving $m_0^2 s \simeq \xi F^2/(4 f_\Phi)$ and substituting into the quadratic Lagrangian. With a matched $+\Phi c_X X/M^2$ term the same elimination yields a cross coefficient $\xi c_X/(4 f_\Phi^2 m_0^2 M^2)$ for XF^2, plus X^2 and derivative terms. Equation (8) makes light-by-light or polarization constraints applicable in the specified limit. The Euler–Heisenberg photon operators provide the radiative Standard Model baseline. A finite background changes the canonical photon normalization and the validity of the expansion. For scalar-independent gauge charge, local canonical normalization gives $e_{\text{eff}} \sim e/\sqrt{Z}$ in a neighborhood of nearly constant Φ. Extrapolating to very small Z needs a perturbative-control check. R02 R06

An EFT prediction at a chosen order needs a power counting, a regulator that preserves gauge symmetry, a complete basis for the retained symmetries, and SMEFT or low-energy matching at a specified scale. Loop insertions mix into other allowed operators. A single universal beta function for α cannot be read from the June action without stating species, charge, basis, scheme, and accompanying coefficients. Perturbative unitarity restricts amplitudes as the energy approaches the effective cutoff. In a Wilsonian calculation the finite set of coefficients at each order can be renormalized and fitted. The archived string, asymptotic-safety, and E_8 ideas are potential high-energy contexts. Their relation to this EFT depends on actual matching data. A1 A6 R03

4 A solved ESFD instability

4.1 Equilibrium and the two stability questions

Use the independent branch of (4) with flat metric, uniform background $\mathbf{B} = B\hat{\mathbf{z}}$, zero electric field, no transport current in the local volume, and $V(\Phi) = f_\Phi^2 m_0^2 \Phi^2/2$ with $m_0 > 0$. The external source and mean flux are assumed fixed for the local perturbation problem. A time-independent scalar minimizes $V_B = V + ZB^2/2$ at prescribed B. Define $x = \xi\bar{\Phi}$. The equilibrium equation and fixed-field scalar curvature are

$$xe^x = \frac{\xi^2 B^2}{2 f_\Phi^2 m_0^2}, \qquad m_B^2 = \frac{V''(\bar{\Phi}) + Z''(\bar{\Phi}) B^2/2}{f_\Phi^2} = m_0^2(1+x). \tag{9}$$

For the real branch $x = W_0(\xi^2 B^2/(2 f_\Phi^2 m_0^2)) \geq 0$ this scalar curvature is positive. At fixed magnetic excitation $H = ZB$ the local magnetic Legendre potential is $V - H^2/(2Z)$, whose curvature per f_Φ^2 evaluates to $m_B^2 - g_B^2$, with $g_B = Z' B/(f_\Phi \sqrt{Z})$. Equivalently this is the Schur complement of the magnetic block in the local Hessian. The choice of which magnetic perturbations are permitted changes the question. The appropriate Hamiltonian or energy principle for a real system must account for its sources, flux constraints, plasma, and boundary energy.

4.2 Mixed modes and onset

For $\mathbf{k} = k\hat{\mathbf{x}}$ there is a photon polarization A_y whose magnetic perturbation has a component along the background. Define $p = \sqrt{Z}\,\delta A_y$ and $s = f_\Phi \delta\Phi$. The quadratic Lagrangian contains the mixing $-g_B s\,\partial_x p$. The other transverse polarization has no such term in this geometry. For an angle θ between $\mathbf{k}$ and $\mathbf{B}$ the determinant in the mixed subspace is

$$(\omega^2 - k^2)(\omega^2 - k^2 - m_B^2) - g_B^2 k^2 \sin^2\theta = 0. \tag{10}$$

Let $g_\theta = |g_B \sin\theta|$. The two real eigenvalues in ω^2 are

$$\omega_\pm^2 = k^2 + \frac{m_B^2}{2} \pm \sqrt{\frac{m_B^4}{4} + g_\theta^2 k^2}. \tag{11}$$

For $g_\theta > m_B$ the lower branch is negative for $0 < k < \sqrt{g_\theta^2 - m_B^2}$. Its maximum growth rate is $\gamma_{\max} = (g_\theta^2 - m_B^2)/(2g_\theta)$ at $k_{\max}^2 = (g_\theta^4 - m_B^4)/(4g_\theta^2)$. The positive kinetic Hessian and the relativistic principal part are preserved. This is an energy instability of a coupled background and precedes any nonlinear saturation analysis. Plane waves parallel to the background have $g_\theta = 0$. For a cubic periodic domain aligned with a transverse wave vector, at least one mode fits when $2\pi/L < \sqrt{g_\theta^2 - m_B^2}$. Other boundaries can change both the spectrum and the magnetic constraints.

For the quadratic potential, $g_B^2 = 2m_0^2 x$. The first threshold for transverse propagation is $x = 1$ at

$$B_c = \frac{\sqrt{2e}\, f_\Phi m_0}{|\xi|}, \tag{12}$$

where e in (12) is Euler's number. At $B = 3B_c$, $x = 2.34496$, the unstable transverse band ends at $k = 1.15972\, m_0$, and $\gamma_{\max} = 0.31052\, m_0$ at $k = 0.75898\, m_0$. At this field, unstable wave-vector orientations are possible for $|\sin\theta| > 0.845$, about 57.6° or farther from either orientation along the field. A periodic transverse domain needs $Lm_0 > 5.42$ for a mode to fit. We separately integrated the two coupled second-order mode equations with an initial displacement having both normal-mode components and zero velocity. The projection on the unstable eigenvector agrees with the predicted $\cosh(\gamma_{\max} t)$ to approximately 2.3×10^{-12} relative error on the sampled grid. This is a dimensionless calculation with chosen initial data and convergence tolerances.

A simple test of medium suppression gives the transverse photon an effective gap ω_p in the diagonal of (10). The unstable sign requires $g_\theta^2 > (k^2 + \omega_p^2)(k^2 + m_B^2)/k^2$. The minimum of the right

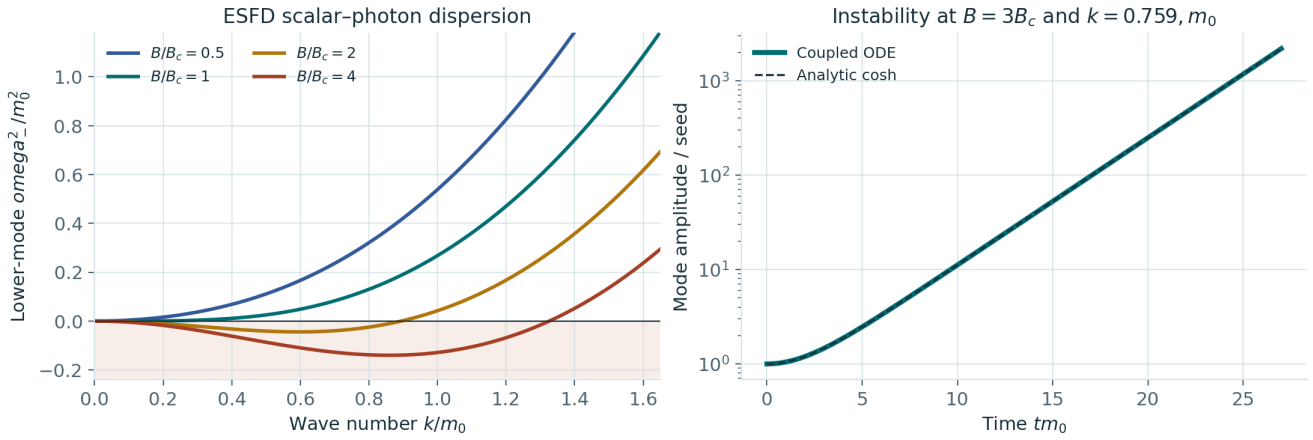


Figure 2. The ESFD independent-scalar threshold. The negative squared-frequency band appears above the transverse threshold. The second panel compares a direct integration of the mixed modes with the analytic growth rate. The calculations use m_0 as the frequency and wave-number scale.

side is $(\omega_p + m_B)^2$ at $k^2 = \omega_p m_B$ when both masses are positive. A positive gap can therefore close the unstable band. Magnetar matter requires an anisotropic response matrix with realistic conductivity, charge density, and plasma and QED polarization. The simple gap is an illustrative modification of the determinant. A stellar prediction additionally requires numerical values of $f_\Phi m_0/|\xi|$, an emission map, and a physically matched source of Φ, including its spin dependence. At zero coupling the modes approach a free photon and a free massive scalar. At high fields a perturbative gauge description and the physical sources of the background must be checked.

The electron QED field provides a unit conversion, $B_Q = m_e^2/|q_e| \simeq 8.62 \times 10^{11}$ eV^2 for 4.414×10^{13} G. For illustration, a transverse $B_c = 10^{15}$ G would need $f_\Phi m_0/|\xi| \simeq 8.4 \times 10^{12}$ eV^2. Choosing $f_\Phi/|\xi| = 10^9$ eV would then imply $m_0 \simeq 8.4$ keV, an inverse mass length $\hbar c/m_0 \simeq 2.4 \times 10^{-11}$ m, and a growth time $\hbar/(0.3105 m_0) \simeq 2.5 \times 10^{-19}$ s at $3B_c$. These are illustrative scales. Assigning the same onset to a stellar flare requires independently matched coupling and plasma physics and a mechanism by which a local mode drives a macroscopic event.

4.3 An independent laboratory check on the onset scale

At weak field, the lower transverse branch of (11) has $\omega^2/k^2 = 1 - g_B^2/m_B^2$ in the long-wavelength limit. Only the polarization with its wave magnetic field aligned to the background mixes at this order. For a transverse external field that wave's electric polarization is perpendicular to the background. With $C_F = \xi^2/(32 f_\Phi^2 m_0^2)$ from (8), its extra index is $n_\perp - 1 \simeq 16 C_F B^2$. The other polarization has no such leading scalar contribution. The tie between the low-energy coefficient and strong-field threshold is $C_F B_c^2 = e/16$, which gives the signed prediction

$$\delta(n_\parallel - n_\perp) = -16 C_F B^2 = -e(B/B_c)^2. \tag{12a}$$

The published PVLAS result at 2.5 T is $(12 \pm 17) \times 10^{-23}$, with QED expectation 2.5×10^{-23}. Treating the published error as approximately Gaussian and using the lower endpoint of a two-sided 95% residual interval gives $\delta(n_\parallel - n_\perp) \gtrsim -2.38 \times 10^{-22}$. Under the stated weak-field, low-energy, adiabatic vacuum assumptions and with this one extra coefficient, it gives $B_c \gtrsim 2.67 \times 10^{15}$ G. A proposed vacuum onset $B_c = 10^{15}$ G would give -1.70×10^{-21} at 2.5 T and lie about 10.6 published

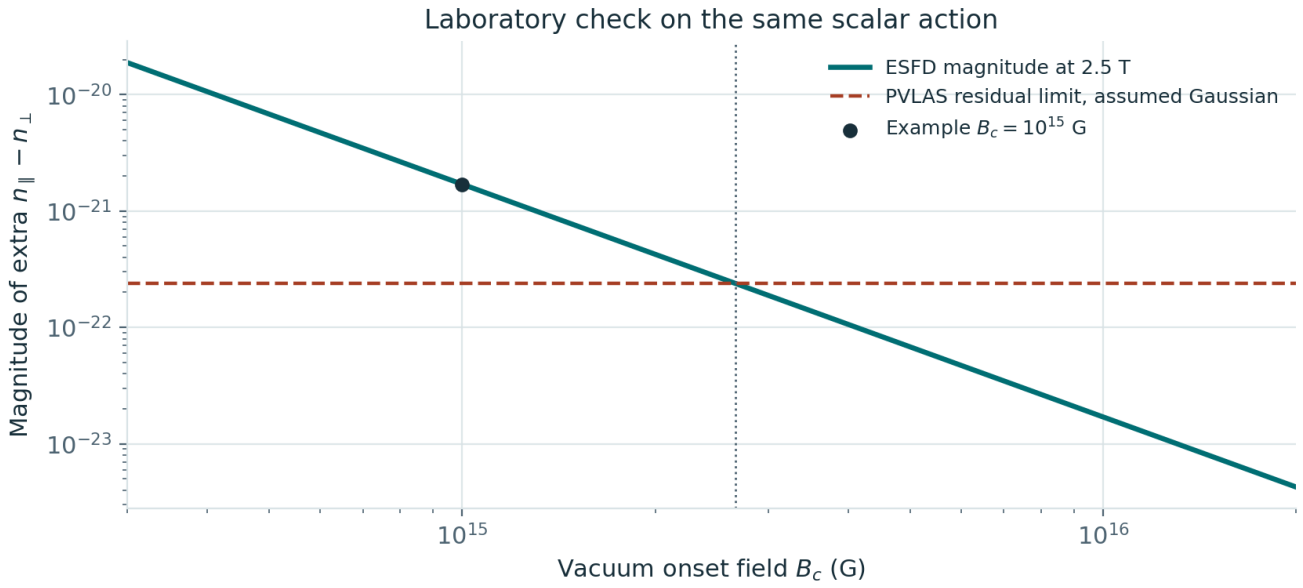


Figure 3. The extra birefringence in the minimal ESFD scalar action and the conditional PVLAS limit. The measurement was made at 2.5 T. The horizontal axis gives a candidate strong-field onset for the same action.

standard errors below the observed central value after adding QED. This is a calculation from the published summary, with the ordinary QED expectation held fixed. Additional optical operators, nonuniform backgrounds where the scalar does not equilibrate, or medium-only couplings require a new propagation analysis. The concrete result is a cross-regime test of the same proposed action without a fitted stellar parameter. R60

4.4 How spin can move the threshold in matter

Let a locally uniform prescribed spin source enter as $+j_s\Phi$. An example is $j_s = c_X\langle X\rangle/M^2$ in the operator convention above. Here j_s has units of energy density and $\langle X\rangle$ is a renormalized, medium-specific correlation. If the source is held fixed in the mode calculation, define $x_s = \xi j_s/(f_\Phi^2 m_0^2)$ and $y = x - x_s$. The background solves $ye^y = \xi^2 B^2 e^{-x_s}/(2f_\Phi^2 m_0^2)$ and the dispersion uses $m_B^2 = m_0^2(1+y)$ and $g_B^2 = 2m_0^2 y$. The no-plasma transverse onset becomes $B_c(j_s) = B_c(0)e^{x_s/2}$. If $B_c(0)$ saturates the conditional PVLAS bound, an onset at 10^{15} G in matter would require $x_s \simeq -1.96$ or more negative, under this particular uniform-source model. The needed backreaction and sign can be calculated once a spin susceptibility and operator matching are supplied. A real compact-star medium has a fluctuating spin source and a plasma response, so a quantitative application must include their variations in the mode matrix.

4.5 Nonlinear endpoint and numerical continuation

Equation (12) determines onset within this toy model. The growing eigenvector consists of correlated scalar and magnetic perturbations. To determine the endpoint, fix a conserved flux $\int B\,dA$, specify the scalar potential away from its minimum and Z over the explored range, and minimize or time-evolve the coupled fields with sources and losses accounted for. In a periodic box the next reproducible checks are the predicted finite-domain threshold, modes on both sides of it,

and convergence of the flux and total energy under refinement. Boundary conditions must allow the magnetic component of the eigenvector and retain comparable background energy. A magnetic domain, an unbounded local response in a fixed-source model, a radiating transient, and collapse of a self-gravitating object have different criteria.

A saturation term of the form $\lambda_\Phi f_\Phi^4 \Phi^4/4$ changes the criterion through V''. A constitutive torque law or $\Phi = C(X)$ has a different linearization. An appropriate route to a rotating-object calculation is a local equilibrium and stability comparison at known field, followed by a rotating multifluid equilibrium and, if the effect survives, a constrained 3+1 evolution. The code in this release solves the reduced Fourier mode system. The older archive describes FDTD, spinning-ring, spin-fluid and magnetosphere tests for which the original numerical models and records are still unavailable. A2 A6

5 Laboratory spin, phase, and inertia

5.1 Spinning tops and preferred environmental alignment

Grenke's earliest examples involve a top, a lighter, and a rotor losing stability when driven away from a local rotational habit. A symmetric top obeys $\dot{\mathbf{L}} = \boldsymbol{\tau}$ and in fast, nearly steady precession $\Omega_{\text{prec}} \simeq Mgd/L$. Euler rigid-body equations predict free wobble and intermediate-axis instability. Contact friction, motion of the contact point, shifting moments of inertia, eddy currents, ferromagnetic hysteresis, the angular distribution of a drive, and support resonances give distinct losses and bifurcations. For ordinary eddy-current braking at low speed one often obtains a dissipative torque that is odd in rotation and even under magnetic field reversal. Purely mechanical instability at matched field-off conditions defines a control. A fixed preferred cosmic direction would introduce a measurable directional dependence and is already subject to precision polarized-spin torsion-pendulum tests. A1 A6 R27

A workable rotational-inertia test models the coupled energy and dissipation. With I fixed, $I\dot{\Omega} = N_{\text{drive}} + N_{\text{environment}} + N_{\text{proposed}}$. If a local preferred direction is represented by a physical axial vector $\mathbf{b}$, the scalar $\Omega_b = \boldsymbol{\Omega} \cdot \hat{\mathbf{b}}$ supplies a directional regressor. Its interpretation requires identifying $\mathbf{b}$ from a local, independently measured field or a specified frame and stating the time and orientation dependence. For a pure reversible interaction $-\lambda\, \boldsymbol{\Omega} \cdot \mathbf{B}$ the observable is a change to canonical angular momentum and forces under gradients. A dissipative torque also requires degrees of freedom that absorb angular momentum and heat. The full apparatus, mount, and surrounding field enter the balance.

In a rotating frame the ordinary spin–rotation Hamiltonian includes $-\boldsymbol{\Omega} \cdot \mathbf{S}$, in addition to the orbital term. A spin with gyromagnetic ratio γ_s behaves in a Barnett field of scale Ω/γ_s in that sense. The reciprocal Einstein–de Haas response transfers changes in magnetization to mechanical angular momentum. These effects supply positive checks that a test is sensitive to spin conversion. A neutral body gives a particularly useful comparison between bulk inertia, a polarized ensemble, and a field acting directly on the supports. Changes in stored energy contribute their own E/c^2 to a closed system's rest mass.

5.2 Clock law, historical units, and a reversal test

The early time-feedback branch proposes expressions such as $d\tau/dt = e^{-\xi\Phi_{\mathrm{EM}}}$ or $e^{-\alpha S:F}$. In (1), $\alpha S : F$ has dimension four, so a separate normalization is required even for a phenomenological exponential clock factor. In the covariant scalar action Z explicitly multiplies the photon kinetic term. Clock frequencies, signals in an optical link, and the metric proper time depend on specified couplings and trajectories. A spin-dependent shift is naturally sought in a transition Hamiltonian or in a defined matter metric. Under a universal conformal scalar factor $\tilde{g}_{\mu\nu} = A(\Phi)^2 g_{\mu\nu}$, massive clocks coupled to $\tilde{g}$ measure $d\tilde{\tau} = A\, d\tau_g$. Local ratios of clocks sharing the same metric require transport and redshift modeling to separate the effect. Nonuniversal coupling generally gives species- and binding-energy-dependent shifts. A1 A6 R23 R24

The June rotor example specifies 4 T and 5.0×10^3 rad/s. The printed $\chi_{\mathrm{tim}} \approx 0.32$ evaluates to 3.18×10^{-7}. A hypothetical clock carried at the 0.10 m rim would move at 500 m/s and have an ordinary leading fractional SR shift $-v^2/(2c^2) \simeq -1.39 \times 10^{-12}$, or -1.20×10^{-7} seconds per day. A stationary reference looking at a rotating mirror measures an optical transfer response whose Doppler, Sagnac, path length, and birefringence terms depend on the geometry. The manuscript's target excess 10^{-10}–10^{-9} seconds per day corresponds to a fractional effect of 1.16×10^{-15}–1.16×10^{-14}. It remains an archived sensitivity target without a matched signal law at the corrected index. A1 R24

Define the response $y = \delta\nu/\nu$ of a specified transition or a calibrated torque channel. Under independent sign flips $\epsilon_B, \epsilon_\Omega, \epsilon_s \in \{-1, +1\}$ of field, bulk rotation, and spin polarization, the coefficient of the term odd in B and Ω and even in spin polarization is $\hat{y}_{B\Omega} = \frac{1}{8}\sum \epsilon_B \epsilon_\Omega y(\epsilon_B, \epsilon_\Omega, \epsilon_s)$. Define analogous contrasts for the other parities before seeing outcomes. Randomize reversal order and blind the contrast used to test the model. A differential measurement can fit $y = y_{\mathrm{known}}(\mathbf{x}) + c\, f(B, \Omega, \mathbf{M}, \theta) + \epsilon$, with $\mathbf{x}$ including temperature, field gradients and vibrations. Use zero rotation/zero field rows, unpolarized material controls, two transition sensitivities, and time-dependent ambient and magnetic controls. Limits constrain the declared function and coefficient. The old proposal $\delta\omega/\omega_L = a_1\chi_{\mathrm{tim}}^2 + a_2\chi_{\mathrm{tim}}^3$ requires independent coefficient predictions and separate parity definitions for each term. A6

5.3 Neutral-particle phase and condensed-matter benchmarks

The Aharonov–Casher phase of a magnetic dipole following a path in an electric field is, in SI for a fixed moment and the appropriate ideal geometry,

$$\Delta\varphi_{\mathrm{AC}} = \frac{1}{\hbar c^2}\oint (\boldsymbol{\mu} \times \mathbf{E}) \cdot d\ell. \tag{13}$$

A line charge λ_e and a transverse circular path with axial moment μ yield $\Delta\varphi_{\mathrm{AC}} = \mu\lambda_e/(\epsilon_0\hbar c^2)$, using the sign of the winding and dipole. Radius independence follows from the $1/r$ electric field and circumference. A reversed winding or spin reverses the phase. The neutron and atom interferometry comparisons in the old discussion therefore have a quantitative quantum baseline. A proposed ESFD phase needs a distinct prediction for geometry, field dependence, polarization, or energy, checked against electric polarizability, dynamical phase, and geometric controls. Phase coherence in a neutral beam does not require a new mechanical drag law. A6 R07

Stern–Gerlach separation, Ramsey precession, nuclear magnetic resonance, the spin Hall effect, spin–orbit torque, and magnetization dynamics are controlled cases for estimating a spin re-

sponse. For spinor Bose condensates a spin-ordering energy, Zeeman terms, density interactions, and trap geometry already permit instabilities and loss of coherence. If a new coupling is proposed, compare $\delta g_s n$, its sign, or a specified mode eigenvalue with the ordinary spin-dependent scattering energy and chemical potential. Without that matching an archived condition $U_{\mathrm{ESFD}} \gtrsim \mu_{\mathrm{BEC}}$ has free normalization. NV-center magnetic readout and spintronics provide useful reversal and noise calibration. They probe specific effective coefficients in their medium. A tokamak or laser experiment similarly needs a plasma equilibrium, ordinary reconnection and radiation-pressure predictors, and a residual observable sensitive to a spin-dependent term. A1 A2 A6

6 Pulsars, magnetars, and flares

6.1 The original line on the timing data

The rebuilt ATNF snapshot contains 4,503 objects. The timing subset is the 2,898 with finite $P > 0$ and $\dot{P} > 0$. There are 1,524 missing period derivatives and 81 supplied nonpositive derivatives. Treat the latter separately because cluster acceleration, kinematic contamination, and measurement noise can enter observed $\dot{P}$. The dipole proxy is the standard equatorial vacuum-convention value $B_{\mathrm{tim}} = 3.2 \times 10^{19}\sqrt{P\dot{P}}$ G for P in seconds. Fix the old normalization before looking at the labels. Writing $\tau_c = P/(2\dot{P})$,

$$\chi_{\mathrm{tim}} = \frac{2\pi(3.2 \times 10^{19})}{\Lambda_{\mathrm{tim}}}\sqrt{\frac{\dot{P}}{P}} = \sqrt{\frac{\tau_*}{\tau_c}}, \qquad \tau_* = \frac{1}{2}\left(\frac{2\pi(3.2 \times 10^{19})}{\Lambda_{\mathrm{tim}}}\right)^2 = 1624.076\,\mathrm{yr}. \tag{14}$$

The numerical identity is satisfied to a maximum reported relative discrepancy of 5.6×10^{-16}. The rank ROC AUC for the ATNF AXP label is 0.9367 for both χ_{tim} and inverse characteristic age. The field proxy has AUC 0.9965 and mean precision over its recall ladder of 0.9143 in this retrospective sample. The high scores reflect the selected labels, population and timing assumptions. They do not supply out-of-population predictive accuracy. At the fixed cut there are 5 tagged passes, 17 tagged misses, and 4 other passes. The descriptive Wilson 95% interval for the tagged pass fraction is 0.101–0.434. Removing the catalogued globular-cluster objects leaves the 5 and 4 counts intact. Among 485 other objects with a matched intrinsic period-derivative estimate, the correction does not change their threshold side. R05 R08

The McGill snapshot lists 24 confirmed magnetars, six candidates, and one outburst pulsar. Twenty-two confirmed sources have uncensored positive timing for this calculation. Five pass the fixed line. Two of the three giant-flare hosts are above it at the selected catalog timing epoch, and SGR 0526−66 is below at $\chi_{\mathrm{tim}} = 0.695$. SGR 1806−20 and SGR 1900+14 give approximately 2.59 and 1.35. Event-time timing and monitoring exposure differ from catalog epochs and are required for a per-event necessary-condition test. The Crab is a rotation-powered pulsar above the line at $\chi_{\mathrm{tim}} \simeq 1.14$. Its nebular gamma-ray flares occur in a different emitting region than a magnetar surface or magnetosphere. The young pulsar J1846−0258 gives a productive intermediate case because a magnetar-like event was observed. SGR 1935+2154 provides a separate magnetar/radio-transient example. The two catalog samples overlap. R08 R09 R10 R11

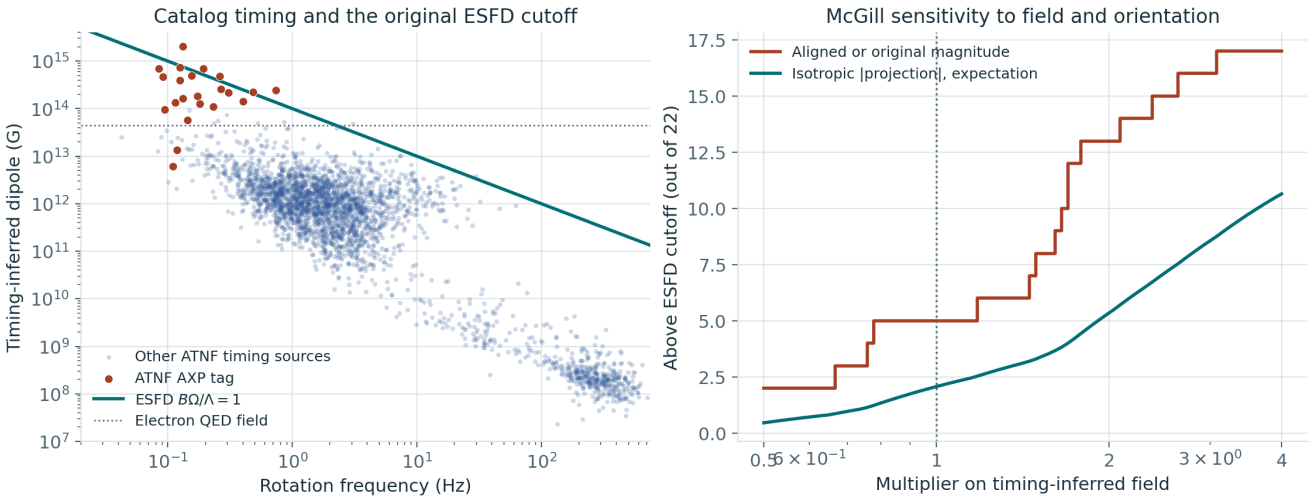


Figure 4. ESFD cutoff explicitly overlaid on ATNF timing data, with the field-scale and orientation-sensitivity calculation for confirmed McGill magnetars. The field coordinates use a timing convention. The right-hand expectations use an illustrative isotropic distribution of angles.

6.2 Orientation and the observed high-field, fast-spin gap

A signed or magnitude-projected threshold can be written $s_B \chi_{\rm tim} \cos\theta$ or $s_B \chi_{\rm tim} |\cos\theta|$, with s_B an assumed field multiplier. For an isotropic independently distributed orientation relative to $\boldsymbol{\Omega}$, $|\cos\theta|$ is uniform on $[0, 1]$. The resulting expected pass probability is $\max(0, 1 - 1/(s_B \chi_{\rm tim}))$ in the magnitude version, and half this for a positive signed cut. Each expectation is the sum over the catalog. At $s_B = 1$ the expected number of McGill passes is 2.07 in the magnitude version, compared with five for the scalar product of magnitudes. At $s_B = 2$ the expected number rises to 5.35, while the aligned or magnitude limit gives 13. For ATNF tags the respective $s_B = 1$ counts are 1.60 expected and five magnitude passes. Orientation or obliquity inference in an actual population needs a different distribution linked to the torque and selection. A projection with multiplier fixed at unity can only reduce the count, point by point. The sensitivity analysis is new and fully reproducible.

Among the eligible ATNF sources the region $P \leq 0.1$ s and $B_{\rm tim} \geq 10^{13}$ G is empty. That is a genuine catalog observation. Birth distributions, short crossing or residence times, field evolution, torque prescriptions, beaming and radio surveys, intermittency and X-ray selection can contribute to the observed occupancy. A force-free spin-down law in the usual dipole notation has $\dot{E}_{\rm sd} \sim \mu^2 \Omega^4 (1 + \sin^2 \alpha_{\rm ob})/c^3$. It gives a nonzero aligned spin-down and changes the mapping from $\dot{P}$ to B relative to the orthogonal vacuum proxy. A hazard or birth-exclusion inference needs a forward population with the relevant selection functions and an age distribution. The empty region by itself supplies no estimate of a universal dynamical boundary. R05 R08 R12

A useful follow-up likelihood conditions on monitored source-time exposure $T_i(t, E)$ and separately models glitch, ordinary burst, giant flare, and radio-transient outcomes. A Poisson intensity, for example $\lambda_i(t) = T_i(t, E) \exp(\alpha_i + \beta^\top \mathbf{x}_i(t) + c_{\rm ESFD} h_i(t))$, permits age, dipole, twist, and activity history to enter separately. Calibrate time-variable spin-down irregularity before evaluating an event. Preselect independent field estimates such as lines with verified identification, phase-resolved emission geometry with model uncertainty, or simulated distinct internal stresses. A timing-based h_i identical to a monotone age transform cannot establish separate age and ESFD

effects without additional structure. Hold out entire sources and later observing time.

6.3 Glitches, energy reservoirs, and timing tests

The rebuilt glitch list has 625 events in 211 objects. The prior-glitch cohort uses 198 with eligible timing and a within-sample recurrence window, yielding 19 repeaters of which 18 sit below $\chi_{\rm tim} = 1$. The age-equivalent AUC is 0.742 and a past-glitch-count baseline gives AUC 0.752 and average precision 0.437, versus 0.220 for $\chi_{\rm tim}$. The recurrence comparison is retrospective and lacks harmonized monitoring exposure. A physically informative model compares pinned-superfluid angular-momentum transfer and crust/magnetospheric reconfiguration, with measured changes in spin frequency and braking. For $\dot{\Omega} = -K(t)\Omega^n$ one obtains $\Omega\ddot{\Omega}/\dot{\Omega}^2 = n + (\Omega/\dot{\Omega})\dot{K}/K$, so timing noise and torque evolution can mimic a new braking index. Quasi-periodic oscillations following giant flares supply a separate magnetoelastic mode diagnostic with uncertain mode identifications. R08 R09 R13

For illustration fix $M = 1.4\,M_\odot$, $R = 12$ km, $I = 0.3MR^2$, and $|W| = 0.6GM^2/R$. The Gaussian estimates $T = I\Omega^2/2$ and $E_B = B_{\rm int}^2 R^3/6$ assume a constant interior field and spherical volume. They give $B_{\rm int} = 9.48 \times 10^{17}$ G or $P = 0.303$ ms when either single term is equated to $|W|$. For $B_{\rm int} = 10^{15}$ G and $P = 5$ s, $(T + E_B)/|W| = 1.12 \times 10^{-6}$. Its illustrative magnetic energy is 2.88×10^{47} erg, above typical burst energies and comparable to the scale contemplated for the largest giant events if even a fraction can be released. The corresponding rotational reservoir is about 9.5×10^{44} erg. Using an illustrative 10^{17} G interior field gives $\chi_E \simeq 0.0111$. At 716 Hz and zero magnetic contribution, $\chi_E \simeq 0.047$. These numbers cohere as energy budgets. Stability depends on magnetic topology, deformation, stratification, cooling, mass shedding, and the equation of state. Flares may draw on local magnetic free energy and cross a reconnection threshold even when $\chi_E \ll 1$. A1 A3 R09 R14

6.4 Strong-field photon propagation and IXPE

The electron field $B_Q = m_e^2 c^3/(e\hbar)$ in Gaussian units is a QED scale independent of rotation. With weak fields and low photon frequency, the Euler–Heisenberg result for propagation at angle θ to the field has $n_\parallel - 1 \simeq 7\alpha_{\rm em}(B\sin\theta/B_Q)^2/(90\pi)$ and $n_\perp - 1 \simeq 4\alpha_{\rm em}(B\sin\theta/B_Q)^2/(90\pi)$. These are low-field expansions. High-field magnetar predictions require the full strong-field dielectric, plasma and vacuum resonances, surface radiative transfer, and line-of-sight geometry. At 1 keV the frequency is 2.42×10^{17} Hz and the angular frequency is 1.52×10^{18} rad/s. Direct substitution corrects the draft's frequency and angular-frequency interchange. The old $\Delta n \propto \alpha S_0/\omega^2$ needs a response tensor with dimensions, dispersion, and Ward identity checked. A competing q^2 form can be predicted from a dynamical scalar or two-form, with polarization specified. A1 R06

For a prescribed, slowly varying $Z(\Phi)$ with Maxwell action, geometric optics yields $k_\mu k^\mu = 0$ and amplitude transport of the form $\nabla_\mu(Z|\mathcal{A}|^2 k^\mu) = 0$ for a source-free ray. Both polarizations share the leading cone. Dynamical mixing as in (10), QED nonlinear terms, or a parity-odd $F\tilde{F}$ coupling yield other signatures. The archived soft X-ray test can thus compare phase, energy, and direction dependent Stokes parameters against a QED, atmosphere, and magnetosphere likelihood. For 4U 0142+61 the timing values give $B_{\rm tim}/B_Q \simeq 3.04$ and $\chi_{\rm tim} \simeq 0.154$. Its measured polarization changes with energy, including substantially different polarization angles across bands. The published polarization is a baseline constraint on emission and propagation. A separate ESFD parameter and an instrument response are required for an ESFD fit. R06 R15

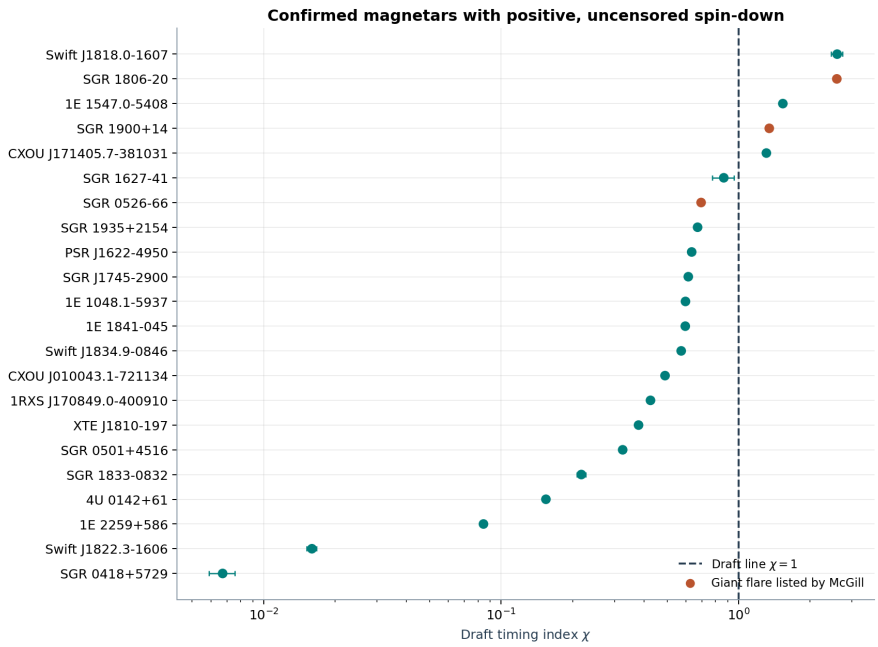


Figure 5. McGill timing relative to the original ESFD line and electron QED field. Spin-down epochs and censoring are discussed in the text.

7 Neutron stars, mergers, and black holes

7.1 TOV, rotation, and matching a spin sector

For spherical perfect-fluid equilibrium in GR with $G = c = 1$,

$$\frac{dm}{dr} = 4\pi r^2 \epsilon, \qquad \frac{dp}{dr} = -\frac{(\epsilon + p)(m + 4\pi r^3 p)}{r(r - 2m)}. \tag{15}$$

Boundary conditions are regular $m(0) = 0$, prescribed central pressure, and $p(R) = 0$. The surface mass is $m(R)$. Six tabulated EOS give 540 equilibria. Their nominal maximum static masses span 2.031–$2.770\, M_\odot$. The AP4 table gives $dp/d\epsilon \simeq 1.34$ at its raw maximum, so that maximum requires a causal EOS treatment. The raw mass-radius curves and sound-speed flags are preserved. A $1.20 M_{\rm TOV}$ proxy illustrates uniform rotational support for a class of EOS. Actual mass shedding, thermal support, differential rotation and magnetic topology depend on the angular-momentum distribution and stability of the remnant. $dM/d\epsilon_c$ along an appropriate sequence is an indicator with hypotheses, and the dynamical boundary can be tested through a radial or nonaxisymmetric mode. Equating a global energy ratio to unity cannot substitute for checking the equilibrium and stability equations. A2 A3 R14 R16

An ESFD stellar model needs an interior $S^{\mu\nu}$, a thermodynamic EOS $p(n, T, Y_e, \ldots)$, composition and transport, a metric, a gauge configuration, and the calibrated relation of the effective spin term to $\delta T^\mu{}_\nu$. If stress is anisotropic, a spherical toy formula gives dp_r/dr an additional $2(p_t - p_r)/r$. In general, rotational/magnetic flattening requires an axisymmetric equilibrium or full evolution. A defensible numerical comparison pairs each ESFD solve with the same baryon mass, angular momentum, initial topology, resolution and EOS in its GRMHD control. Check constraints, surface and asymptotic conditions, gauge dependence and convergence of the proposed observable, such

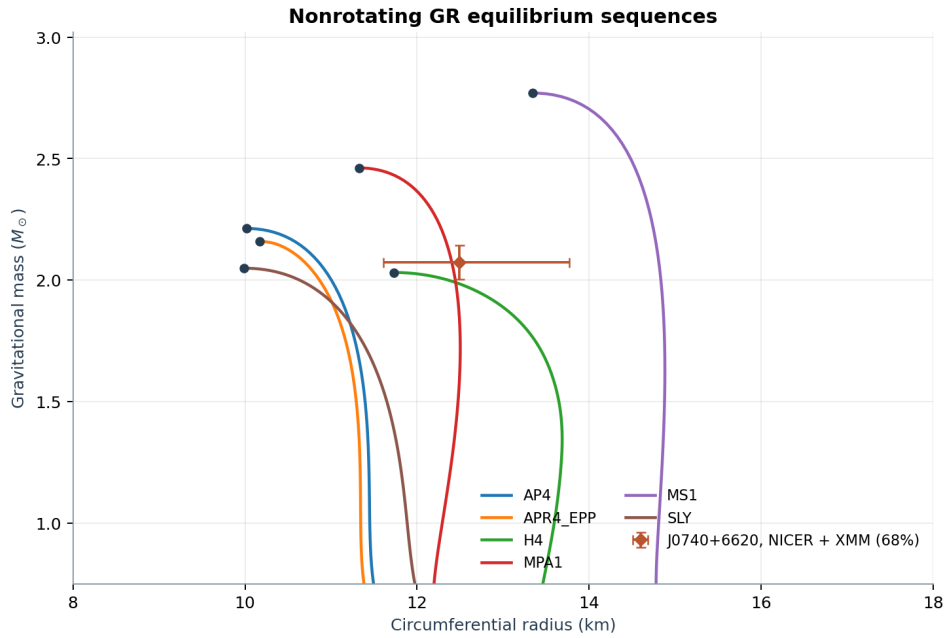


Figure 6. General relativistic stellar benchmark. The integration uses six public tabulated EOS. The AP4 central sound-speed flag applies to its unmodified maximum. A plotted GR sequence supplies the reference for a future matched ESFD stress calculation.

as a shift in mass-radius relation or mode frequency. The GR reference tracks ordinary effects and anchors the $\alpha, \xi \to 0$ limit.

7.2 Kerr spin, observed distribution, and the precursor run

For a Kerr GR black hole $a_* = cJ/(GM^2)$, and its horizon in Boyer–Lindquist radius is $r_+ = (GM/c^2)(1 + \sqrt{1 - a_*^2})$. The horizon angular velocity is $\Omega_H = a_* c^3/[2GM(1 + \sqrt{1 - a_*^2})]$. The Kerr extremal limit $a_* = 1$ follows from the horizon solution. It is used as a control in the historical ESFD extension. An inferred remnant spin is conditional on the waveform and model used to infer it. The cumulative catalog snapshot has 391 distinct confident event summaries through GWTC-5.0, of which 282 have source-frame component medians and intervals. Both listed lower component endpoints exceed $3\,M_\odot$ for 273 of the 282. This count uses the tabulated interval endpoints as an operational mass cut. The uniform-waveform selection from the later PE products yields 189 remnant-spin medians, with median 0.696, 10th and 90th percentiles 0.647 and 0.749. Matched alternate waveform medians differ by 0.0049 in the median absolute difference over 84 pairs. GW190814 and GW230529 illustrate why population, EOS and binary modeling matter near the lower compact-mass boundary. R16 R19

If one inserts Ω_H into the archived timing ratio, the field needed for $\chi_{\rm tim} = 1$ has median about 8.73×10^{11} G in the same remnant subset. This algebraic estimate gives the horizon-threading field at which the timing index would equal unity. In vacuum Kerr the geometry carries angular momentum and a plasma can support currents outside it. The Blandford–Znajek energy-extraction baseline depends on horizon-threading flux and horizon rotation, roughly $P_{\rm BZ} \propto \Phi_B^2 \Omega_H^2 / c$ in one common normalization. An ESFD correction would have to specify horizon flux, disk or jet boundary conditions, charge supply, and an observable such as a residual in the waveform or jet power consistent with those parameters. Horizon flux requires disk and field modeling, independently

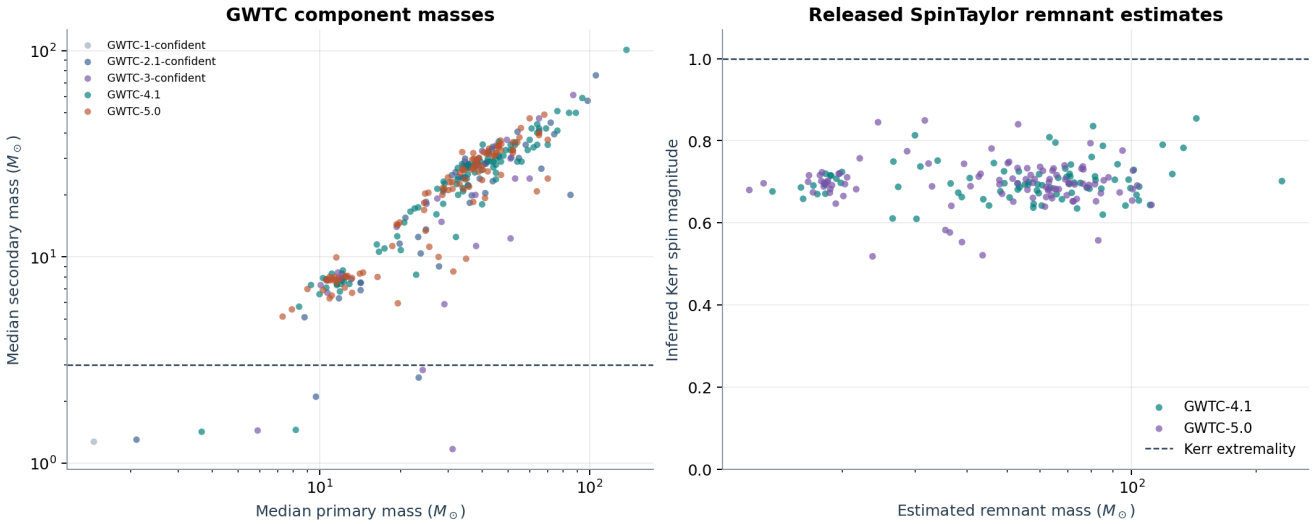


Figure 7. Source mass and waveform-inferred remnant spin distributions from the gravitational-wave data rerun. The displayed spin values are estimated under the selected waveform family.

of pulsar timing. R19 R20

Imaging and long-timescale timing offer complementary controls. EHT ring morphology constrains an exterior metric together with an accretion and emission model. Pulsar timing arrays infer a stochastic background from correlations in timing residuals over the sky. An ESFD signal in either case needs a model for the change in the null rays or the waveform and a covariance that includes the ordinary astrophysical population. Neither observable directly samples an interior spin density. R59

The archived BNS hypothesis predicts a polarized flash between 5 and 0.5 ms before coalescence, with a roughly 90° polarization-angle change. The GW170817 count-space check uses 872,114 raw Fermi/GBM entries across NaI 1, 2, and 5, with 465,709 photons after the pipeline's 10–50 keV channel-center selection. The nominal 4.5 ms window gives counts 2, 1, and 2. The pooled off-source expectation is 8.00 versus five observed. The one-sided excess probability under that Poisson reference is 0.900. An offset scan reaches 13 counts and has an empirical tail probability about 0.947 against 432 off-source control centers. A post-coalescence burst control shows the expected count excess. Clocks, propagation, localization, response matrices, and source timing assumptions delimit this one-event check. Polarimetry, energy fluence limits via response folding, and a population incidence constraint require additional data and calibrated injection recovery. A claimed 22 Hz precursor in another burst, for example the archived GRB 211211A lead, must be tested with that event's data, red-noise nulls, and a prespecified frequency or trials correction. A1 A6 R21 R22

8 Gravity, geometry, and the spin–entropy proposal

8.1 What a derivation of emergent gravity would have to produce

The early proof branch argues that constituent spin and electromagnetic field energy make mass and that long-range spin alignment accounts for inertia and attraction. The later regime-focused

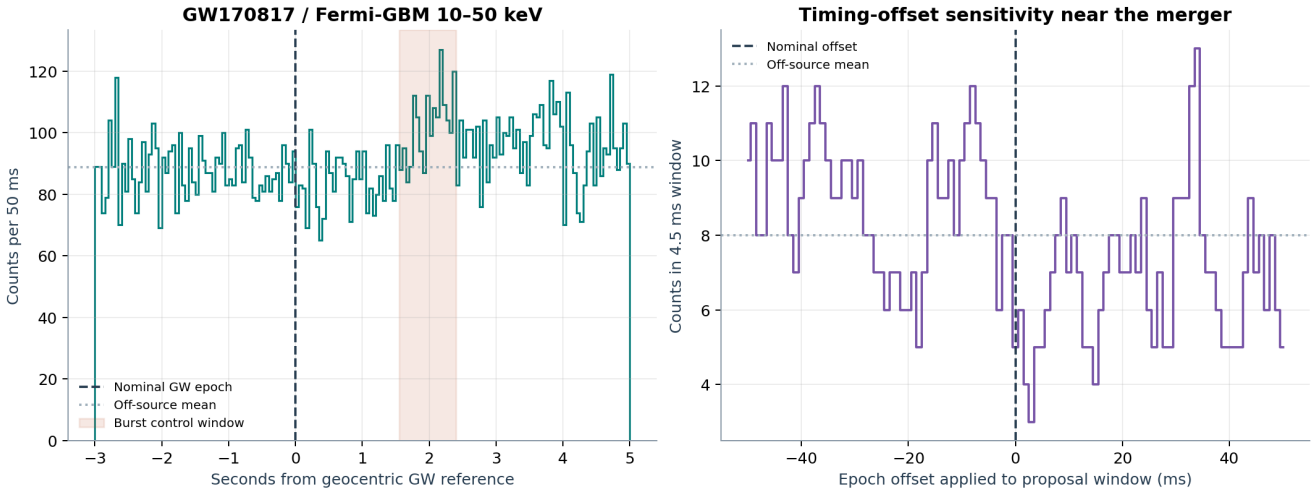


Figure 8. Fermi/GBM count-space test for the old ESFD precursor window in GW170817. The window and offset trials use the same instrument selections. This plot is an intensity test with a single event.

version asks when electromagnetic stresses matter for gravitationally bound systems. In standard GR a localized electromagnetic or spin-dependent interaction contributes through the conserved stress-energy of the complete system. Bulk angular momentum gives gravitomagnetic terms in the exterior metric. Static attraction, light deflection, redshift, inertial response, post-Newtonian corrections, and radiation are additional linked predictions. A derivation of gravity from spin goes beyond computing corrections in an action containing the Einstein–Hilbert term. A4 A6 R23 R25

At distances large compared with neutral source sizes, a static ordinary magnetic dipole pair has energy proportional to $[\boldsymbol{\mu}_1 \cdot \boldsymbol{\mu}_2 - 3(\boldsymbol{\mu}_1 \cdot \hat{\mathbf{r}})(\boldsymbol{\mu}_2 \cdot \hat{\mathbf{r}})]/r^3$ with both signs. Newtonian gravity requires a monopole $-GM_1M_2/r$ whose coupling survives for neutral, unpolarized bodies and for photons in the relativistic description. Polarization variance can be nonzero at zero mean. Its contribution is still set by the range, density scaling and tensor structure of the interaction. A physical source strength and universal charge must be derived. The proof draft's illustrative $G_{\text{naive}} = \alpha_{\text{em}}\hbar c/m_p^2$ is dimensionally possible and numerically 8.25×10^{25} in SI. It exceeds the measured G by about 1.24×10^{36}. It establishes a normalization problem, even before one confronts equivalence. A4

A light scalar with object-dependent charges q_A, q_B gives $U = -q_A q_B e^{-m_s r}/(4\pi r)$ at tree level in natural units. To emulate an extra universal attraction, q_A/M_A must match across compositions and environments or acquire an explicitly modeled screening dependence. Equivalence-principle experiments such as MICROSCOPE compare freely falling materials and bound differential accelerations at the few-10^{-15} scale. Spin-polarized torsion balances constrain orientation-dependent forces for specified ranges and couplings. A putative gravity replacement also has to match photon trajectories and post-Newtonian potentials, plus strong-field binaries. Einstein–Cartan spin contact interactions in the minimal theory and Pauli exchange have their own distance and spin structure. Force-range changes and collective condensates require an additional, specified physical mechanism. R01 R23 R25 R27

The archival connections to Mach and Sciama's inertial induction, Haisch–Rueda–Puthoff vacuum inertia, Sakharov's effective curvature term, Jacobson's thermodynamic Einstein equation, Verlinde's entropic proposal, and Cramer's transactional picture are research analogies. They have different assumptions about microscopic degrees of freedom, state spaces, background geometry,

and coarse graining. For example, integrating out matter can generate a curvature term in an effective action, with coefficient depending on particle content and matching, while a Clausius argument assumes local horizon temperature and an area entropy law. Each of these ideas leaves work for an ESFD mechanism. No recovered derivation gives the observed G, the graviton or other appropriate infrared representation, the equivalence principle, and a complete low-energy matter spectrum from spin–EM data. A2 A4 A6 R31 R32

8.2 Spin–entropy Field Dynamics (SEFD)

The June consolidation records a spin-entropy variable s and current J_s^μ, a gradient term, and the proposed coupling $-\beta_s s \nabla_\mu J_s^\mu$. It gives the combined index $\chi_{\text{tot}} = (B\Omega + \kappa_s s\Omega)/\Lambda_{\text{tim}}$, a separate $\chi_s = s\Omega/\Lambda_s$, and an effective density proportional to $\nabla_i(sJ_s^i)$. These are archived chat-level forms. They can be read as an order-parameter proposal. The thermodynamic entropy density, an entropy current, a microscopic spin tensor, and the von Neumann entropy of a reduced state are different quantities. For entropy density measured in units of k_B per volume, s has natural mass dimension three and κ_s has mass dimension -1 for $s\Omega$ to match $B\Omega$. A dimensionless coarse-grained order parameter would require a different κ_s. An actual entropy current has a constrained divergence under constitutive thermodynamics. A6

The archive form is equivalent to $+\beta_s J_s^\mu \nabla_\mu s$ up to a surface term. A test Lagrangian with $+\gamma_s(\partial s)^2 - U(s)$ and prescribed J_s^μ gives

$$2\gamma_s \Box s + U'(s) = -\beta_s \nabla_\mu J_s^\mu. \tag{16}$$

For a dynamical current, vary and specify its degrees of freedom, mutual response and boundary conditions. If $\gamma_s > 0$ and $U'' > 0$ at the background, the isolated scalar has a healthy kinetic term and positive small-perturbation squared mass. A condition $\chi_s \simeq 1$ becomes predictive once a solution, fluctuation operator, and parameter map are supplied. If using entropy as a hydrodynamic field, dissipation and positivity need a compatible physical closure. A reversible microscopic action and an irreversible coarse-grained entropy functional are connected by the reduction, environment, or stochastic model.

The archived effective gravitational density has a strong integral constraint. With a finite, regular, localized radial flux $s\mathbf{J}_s \to 0$ faster than r^{-2}, its integrated divergence vanishes by Gauss's theorem. For the literal fitted profile with outward amplitude Ce^{-r/r_s}, the enclosed effective mass and density are

$$M_{\text{div}}(< r) = 4\pi C r^2 e^{-r/r_s}, \qquad \rho_{\text{div}}(r) = Ce^{-r/r_s}\left(\frac{2}{r} - \frac{1}{r_s}\right). \tag{17}$$

The solution needs a regular center or a core modification. There is a sign change at $2r_s$ and the total tends to zero. An outer $1/r^2$ flux tail gives a finite boundary charge and requires its own origin. An assumed positive exponential density has a positive asymptotic mass when integrated. Some old drafts use both as halo sources. Treating (17) as a projected effective acceleration is mathematically different from claiming the positive energy of a field. Matching the density to a conserved field stress and to light deflection is essential. An entropy-force ansatz $T\nabla s$ supplies a force once T and s are defined. It does not itself predict a radial law, an observed G, or the same coupling for every test body. A1 A6

8.3 Emergent space from waves and hierarchical spin

In the author's later wave-based description, waves organize into atom-like shells, their relationships build larger structures, and successive additions and reorientations could generate geometry itself. A mathematical version starts with constituent degrees of freedom, an algebra of local observables, and an evolution rule. One example to explore would define a weighted graph through a connected two-point function $C_{ij} = \langle O_i O_j \rangle - \langle O_i \rangle \langle O_j \rangle$ for specified spin or phase observables. An emergent graph distance, a normal-mode or correlation spectral dimension, and a continuum limit could then be studied. The state and the mapping from C to distances have to be declared before assessing whether the result has approximate isotropy, Lorentz symmetry, locality, and an Einstein-like response. Choosing a Hilbert-space tensor factorization or a lattice already uses assumptions about adjacency and independence. An apparent geometric shape formed by a wave visual does not select a unique metric. A6 A7

The required cross-scale checks are concrete. At atomic scales a new interaction must preserve Coulomb hydrogen's spectrum, orbital angular momentum and spin–orbit, Zeeman and hyperfine splittings to observed precision. At molecular scales chemistry depends on exchange, bonding, and electronic states. Macroscopic phase order can arise in spins or a superfluid, with a finite stiffness and correlation length. A field that generates long-range geometry would need independent and covariant predictions as that coarse graining changes. A toy spin network, lattice gauge system, or propagating nonlinear order parameter can test aspects of this proposal. Lattice wave propagation in an already assigned space supplies a dynamical analogy. Emergence of the spatial manifold also requires a reconstruction of geometry from relational observables, along with time evolution and clocks that agree on causal order in the tested limit. R31 R32

9 Galaxies, the Great Attractor, and the dark sector

9.1 What the three archived rotation-curve mechanisms predict

The Electromagnetic Universe and associated galaxy drafts propose (i) a direct field or alignment effect, (ii) a positive spin-supported density with a fitted scale, and (iii) the SEFD divergence source. Some chat versions use $\rho_{\text{spin}} \propto [\langle S \rangle \Omega]^2/(\mu_0 c^2)$ with a coupling, or $V^2_{\text{spin}} \propto \chi\, \alpha(r/R_d) V^2_{\text{bar}}$. These require defined units and an independently measured or predicted $\langle S \rangle$, or a replacement stress law. The older wire estimate with $I = 10^{18}$ A and $r \simeq 3 \times 10^{20}$ m gives $B = 6.67 \times 10^{-10}$ T, 6.67×10^{-6} G, and $\chi_{\text{tim}} \simeq 7.1 \times 10^{-36}$ for a typical orbital rate. The earlier 10^5 G and $\chi \sim 10^{-11}$ values were unit and arithmetic errors. The field of a finite return-current geometry should also replace the ideal infinite-wire approximation when predicting observables. A1 A4 A6

The full SPARC snapshot supplied 3,391 measured radii in 175 galaxies. The rebuilt fit requires quality flag at most 2, inclination at least 30°, finite positive radius and velocity errors, positive measured rotation, and positive baryonic V^2. This leaves 3,166 eligible radii in 153 galaxies and 3,032 radii in 131 galaxies with at least eight points. Baryons use signed contribution $V|V|$ and stellar mass-to-light ratios 0.5 for disks and 0.7 for bulges. The paired profiles were fit with diagonal velocity errors and common fitting choices, and a radial extrapolation comparison trained on the innermost $\lfloor 0.7n \rfloor$ radii and held out 967 outer radii in total. Distances, inclinations, mass-to-light systematic errors, radial covariance and population selection matter for a global astrophysical inference. This is an internally comparable curve-fit test on fixed data choices. R28 R29

For $\rho_{\text{exp}} = \rho_0 e^{-r/r_s}$ the enclosed mass is

$$M_{\text{exp}}(< r) = 4\pi\rho_0 r_s^3 \left[2 - e^{-x}(x^2 + 2x + 2)\right], \qquad x = r/r_s. \tag{18}$$

As r increases the mass tends to $8\pi\rho_0 r_s^3$ and the outer speed eventually falls as $r^{-1/2}$. At small r the finite central density gives a solid-body rise. Add to the baryonic squared speed using $V_{\text{add}}^2 = GM_{\text{exp}}(< r)/r$. The fixed historical NGC 2403 example $\rho_0 = 1.7\times10^{-20}$ kg m^{-3}, $r_s = 6$ kpc gives a peak extra speed around 435.7 km/s against a measured peak 136 km/s in this compilation. The earlier fitted examples for NGC 3198 and DDO 154 are addressed with the same fitting code and fixed baryonic choices. A fit with its own ρ_0, r_s per galaxy constrains a shape family. A first-principles ESFD prediction must determine the normalization and spatial structure from spin and field observations or shared parameters.

Profile	Median full-curve RMSE (km/s)	Median outer holdout RMSE (km/s)
Baryons	44.73	55.15
Published RAR control	13.60	11.86
ESFD archived exponential alone	6.34	14.67
Baryons + ESFD archived exponential	5.43	10.13
Baryons + NFW	5.18	7.84
Baryons + pseudo-isothermal	4.25	6.94
Baryons + literal SEFD flux (17)	5.19	8.40

The exponential plus baryons beats NFW on outer RMSE in 52 of 131 galaxies. The paired median per-galaxy excess in RMSE is 4.89 km/s, with a galaxy bootstrap 95% percentile interval of 0.23–7.25 km/s. The fixed published RAR uses overlapping data in its historical calibration, so its comparison supplies a known relation evaluated under the same cuts. The archived Draco scales give $1.68 \times 10^5\, M_\odot$ within 0.295 kpc, compared with about $1.70 \times 10^7\, M_\odot$ inferred under standard kinematics. For Abell 1689 the fixed exponential gives $8.59 \times 10^{14}\, M_\odot$ inside 2.39 Mpc versus a published weak-lensing-derived summary of about $1.87 \times 10^{15}\, M_\odot$. These fixed comparisons use published summaries and do not reproduce a full kinematic or lensing likelihood. A6 R28 R29 R33

9.2 A stronger energy-budget calculation

To measure the scale mismatch for ordinary electromagnetic energy, use the outermost eligible measured radius of each of the 131 matched galaxies and write $v_x^2 = v_{\text{obs}}^2 - v_{\text{bar}}^2$. In a deliberately simple spherical, weak-field mass proxy, $M_x = rv_x^2/G$. Set the volume-average Maxwell energy divided by c^2 equal to the corresponding mass density. This gives

$$B_{\text{rms,req}} = \sqrt{2\mu_0 c^2 \frac{3v_x^2}{4\pi G r^2}}. \tag{19}$$

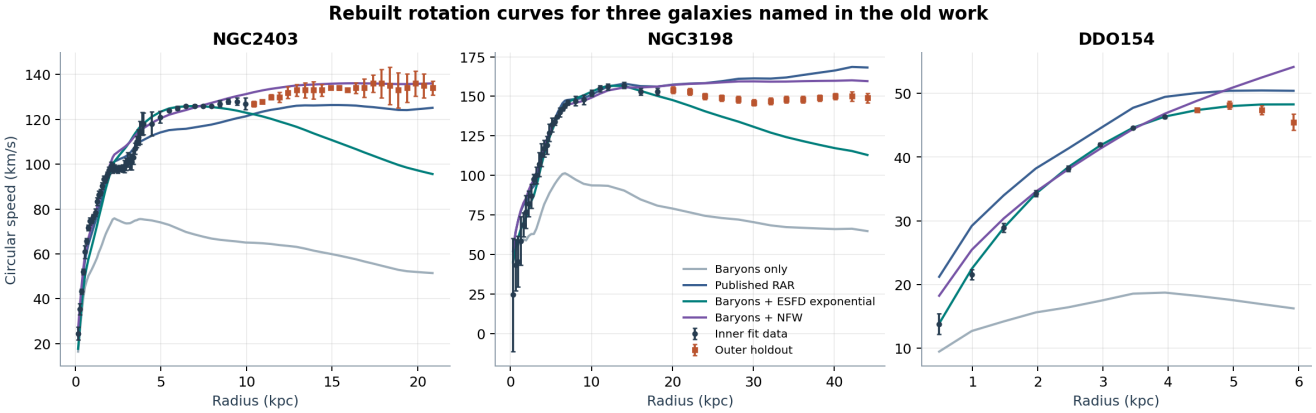


Figure 9. Held-out SPARC radii and inner-fit extrapolations for the three prominently named galaxy examples. The curve labeled exponential in the plot is the archived ESFD profile family in (18).

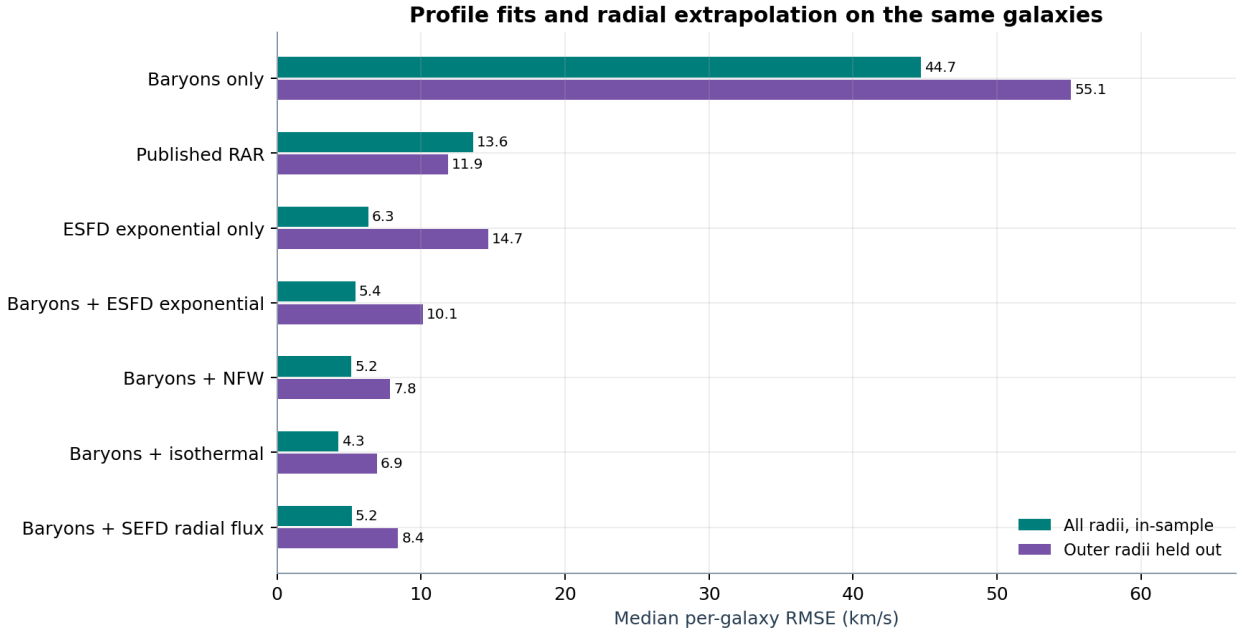


Figure 10. Rebuilt comparison of median galaxy-level residuals. The archival ESFD and SEFD parameterizations appear as the exponential and radial-flux profiles. Both use coefficients fitted to velocity data.

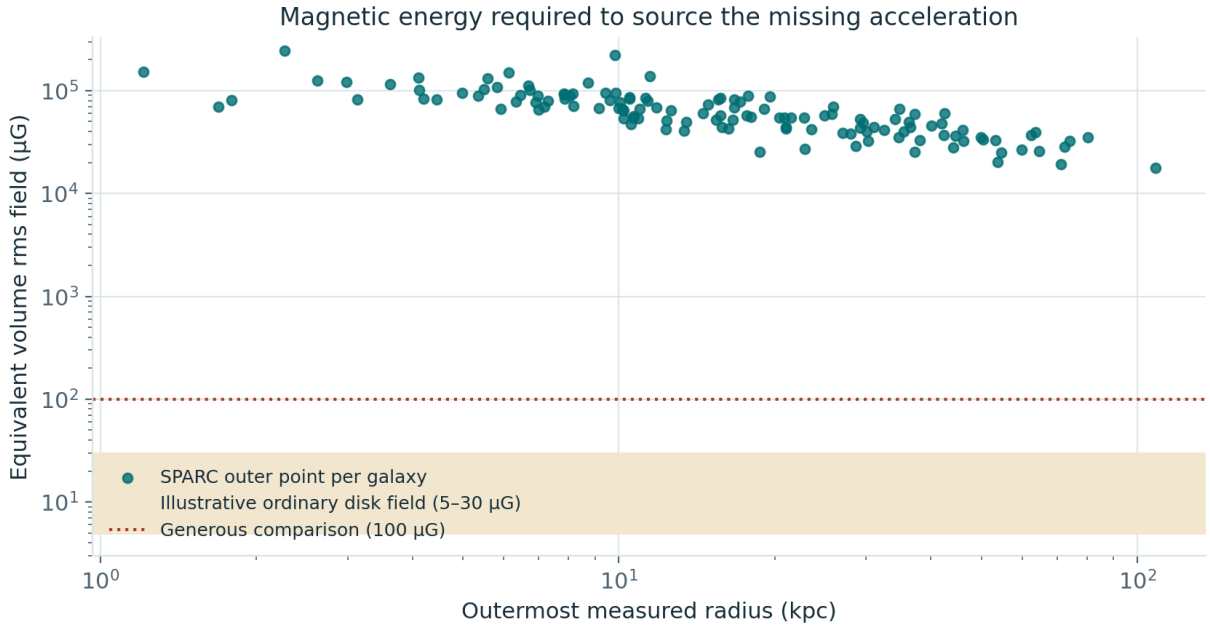


Figure 11. Volume-rms magnetic field that would supply the inferred extra acceleration via ordinary field energy in a spherical mass proxy. One measured outer radius per fitted SPARC galaxy. Comparison bands show assumed field strengths. The plotted points give the required fields.

All 131 selected outer points have positive v_x^2 under the fixed baryonic prescription. The 10th, median and 90th percentiles of the required volume rms field are 3.24×10^4, 5.93×10^4, and 1.04×10^5 μG. For the median point, 10 μG supplies about $1/(3.51\times10^7)$ of this energy budget. Even a uniform 100 μG supplies only about $1/(3.51\times10^5)$. As an example $v_x = 100$ km/s at 10 kpc implies $2.33\times10^{10}\,M_\odot$ and 9.21×10^4 μG. Published spiral-galaxy magnetic studies use synchrotron, polarization and Faraday signals, and ordinary large-scale values are in the μG range. Unknown geometry, anisotropic stresses, volume filling and baryonic uncertainty change (19). The several orders of magnitude in the mismatch cannot be accounted for by an order-unity change to the stress factor. Equation (19) tests gravitation by ordinary measured field energy. A distinct effective field or modified gravity needs its own magnitude from the action. R26 R28

Can the exponential itself close (19)? In the magnetic, quadratic equilibrium of (9), the scalar potential above its vacuum value plus the magnetic energy is $u = V(\bar{\Phi}) + ZB^2/2$. The equilibrium condition gives $V = (x/2)ZB^2/2$, hence $u/u_{\text{Maxwell}} = e^{-x}(1 + x/2)$ at fixed B. For the equilibrium branch $x \geq 0$ this ratio is at most one and decreases, reaching about 0.208 at $3B_c$. This specific exponential response suppresses the local equilibrium energy instead of amplifying it. On a fixed-field energy budget alone, increasing the 10 μG contribution to the median required level would need a factor 3.51×10^7, i.e. a pure multiplicative $Z \simeq e^{17.4}$. That sign and magnitude lie outside the stable homogeneous branch that produced (9). An alternative potential, kinetic energy in inhomogeneous configurations, or explicitly different sourcing of gravity must be developed and checked separately.

For a usable positive ESFD galaxy test, derive a mapping from radio polarization, field reversal, plasma density and vorticity to a prediction for Ψ and Φ_N. A weak-field metric in Newtonian gauge has $g_{00} \simeq 1 + 2\Psi/c^2$ and $g_{ij} \simeq -(1 - 2\Phi_N/c^2)\delta_{ij}$. Slow matter responds to $\nabla\Psi$. Lensing tests transverse gradients of $\Psi + \Phi_N$. A scalar conformal factor can move these potentials in opposite directions and leave null trajectories unchanged for a fixed underlying geometry, even when it

changes dynamics of massive particles. A plasma refraction model also predicts chromaticity. These distinctions are critical in joint gas, stellar-orbit and weak-lensing likelihoods. Begin with galaxies that have matched field and rotation data, fit shared coefficients, and validate on disjoint galaxies with fixed nuisance priors before extrapolating to clusters.

9.3 Cosmic filaments, the Galactic plane, and large-scale flows

The Radcliffe Wave, Galactic disk and supercluster flows connect directly to Grenke's large-scale intuition about organized currents. The Radcliffe Wave is a spatially coherent gas and star-formation structure. Its phase-space motion, vertical velocity and age distribution can distinguish disk gravity and disturbance models. Plasma structures and filamentary magnetic configurations also occur, and morphology alone has weak model specificity. Faraday rotation measures an integral proportional to $\int n_e B_\parallel dl$. Synchrotron intensity and polarization weight electron populations and magnetic fields differently, with foreground and geometry degeneracy. A mechanism claiming that magnetic topology organizes the mass distribution should predict gas, stellar and lensing features with distinct phases or alignment and hold out sky regions. The Great Attractor and Laniakea are first quantified through galaxy peculiar velocities. A field-centered alternative must predict those velocity gradients and a consistent gravitational potential using magnetism data independent of the flows. The localized Galactic magnetic field can affect gas and cosmic rays in a standard approach. A6 R26 R34

A cluster-collision test is essential because the Bullet Cluster shows a separation between much of the X-ray-emitting baryonic plasma and the peaks inferred from weak lensing. A useful prediction specifies the spatial distributions of ordinary gas, collisionless stars and any new spin field before scoring the shear. The old high-redshift rotation, DES or other shear, thermal/kinetic Sunyaev–Zeldovich (SZ), and growth claims need the original samples and predicted covariance, or an independently implemented mechanism with both metric potentials. A scientifically complete alternative should return joint residuals for redshift and scale bins, with covariances, selection, galaxy bias, feedback and projection effects. A circular-speed profile at $z \simeq 0$ has limited reach into these observations. A6 R35

9.4 Early cosmology, magnetogenesis, and dark energy

For statistically isotropic random fields, $\langle B_i B_j \rangle = \langle B^2 \rangle \delta_{ij}/3$. Maxwell stress is traceless and its isotropic coarse-grained equation of state is $p_B = \rho_B/3$ in energy units. Under flux freezing in an expanding background of scale factor a, $B \propto a^{-2}$ and $\rho_B \propto a^{-4}$ for constant Z. A varying Z exchanges energy with the scalar, so the two sectors must be evolved together. The magnetic component has anisotropic stress before the appropriate average, and its contributions to CMB spectra are limited by observations. To behave like cold matter, a proposed spin or scalar component needs sustained clustering with small effective pressure and sound speed on the relevant scales. A coherently oscillating canonical massive scalar with an approximately quadratic potential and $m \gg H$ can have $\langle p \rangle \simeq 0$ in a homogeneous approximation. The perturbations, production and couplings determine whether it is viable. This route adds a dark effective degree of freedom whose properties can be tested. R36 R37

As a background consistency scale, within base ΛCDM the Planck values $\omega_b \simeq 0.0224$ and $\omega_c \simeq 0.120$ with conventional relativistic $\omega_r \simeq 4.18 \times 10^{-5}$ give matter–radiation equality near $z \simeq 3400$. Holding the radiation budget fixed, replacing the matter term by baryons alone gives $z \simeq$

535, after standard recombination. A new theory can change the expansion or add another pre-recombination clustering stress. The required result is a matched calculation of temperature, polarization, peak heights, damping, transfer functions, lensing, BAO and baryon abundance in the alternative model. The archival exponential or SEFD radial flux beside a late galaxy supplies no background stress with these properties. R36

Inflationary magnetogenesis can be explored by evolving $Z(\Phi)$ with the scalar and charged matter. Amplification has backreaction, conductivity, initial state and strong-coupling conditions. A parity-even ZF^2 gauge factor alone does not select one circular polarization at leading fixed-background propagation. Cosmic birefringence can arise with a pseudoscalar coupling $-\frac{1}{4}g_{\varphi\gamma}\varphi F\tilde{F}$ and, in the simple homogeneous slow-background limit, polarization rotation $\Delta\beta = \frac{1}{2}g_{\varphi\gamma}[\varphi_{\rm obs} - \varphi_{\rm em}]$ up to the convention for $\tilde{F}$. Survey calibrations, dust foregrounds and band dependence are required. Any archived order-unity local non-Gaussianity, transfer-function deviation or GW propagation claim needs a defined primordial ensemble and an evolved spectrum, alongside the measured $f_{\rm NL}$, tensor-mode, and CMB constraints. A positive nearly constant scalar potential with small kinetic fraction can mimic vacuum-like $w \simeq -1$. Deriving its magnitude, radiative stability and perturbations is the problem for the dark-energy branch. A6 R36 R37

10 Spin–torsion collapse, white holes, and daughter universes

10.1 A solvable high-density toy model

The early idea treats increasing concentration, spin, and field strength as feedback toward a horizon and then a new phase. In the strongest extension, the high-density core bounces and an expanding region develops on the other side of a global geometry. Start with a toy FLRW patch and a conserved fermion number $n \propto a^{-3}$. Use an effective matter density $\rho_m = mn$ and a negative spin-correlation correction $\rho_s = -\beta_s n^2$, $\beta_s > 0$, motivated by particular averaged spin-fluid treatments, with $p_s = \rho_s$. The sign and magnitude are stipulated here. The quadratic scaling is the essential assumption. For flat geometry and zero vacuum term

$$H^2 = \frac{8\pi G}{3}(\rho_m + \rho_s), \qquad \dot{H} = -4\pi G(\rho_m + 2\rho_s). \tag{20}$$

At the balance $n_b = m/\beta_s$ and $\rho_b = mn_b$, $H = 0$ and $\dot{H} = 4\pi G\rho_b > 0$. Define $t_b = 2/[3\sqrt{(8\pi G/3)\rho_b}]$ and let a_b be the minimum. The result is

$$\frac{a}{a_b} = \left[1 + (t/t_b)^2\right]^{1/3}, \qquad H = \frac{2(t/t_b)}{3t_b[1 + (t/t_b)^2]}. \tag{21}$$

It follows by setting $y = (a/a_b)^3$ and integrating $\dot{y}^2 = 9(8\pi G/3)\rho_b(y-1)$. The expanding branch was independently integrated using the Raychaudhuri equation and $da/dt = aH$, starting at the regular turnaround. The analytic and numerical solutions agree to better than 10^{-9} in the dimensionless scale factor and Hubble parameter over the tested interval. FLRW Ricci and Kretschmann scalars stay finite in this toy solution. Effective negative stiff stress violates the null energy condition near the bounce. Its high-density projection and the validity of the averaged fluid at the balance density require a microphysical model. R01 R38

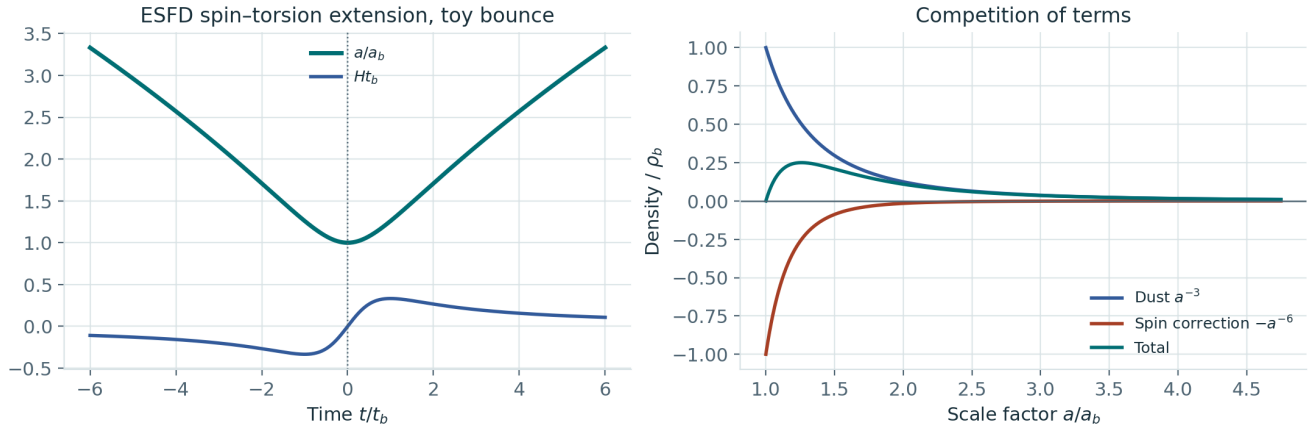


Figure 12. ESFD spin–torsion extension under the chosen homogeneous, isotropic matter and negative-stiff-fluid assumptions. This is the analytic bounce and the two competing density scalings.

A positive shear term in a homogeneous anisotropic model often scales as a^{-6} as well. A bounce driven by the negative spin-fluid term then needs its coefficient to exceed the positive shear contribution in the same Friedmann normalization. For relativistic matter with $\rho \propto n^{4/3}$ the balance density scales as $(\rho/n^{4/3}\beta_s^{-1})^{3/2}$. With an ordinary gravitational-strength contact, the scale is very high. Extrapolation from nuclear densities using a nonrelativistic dust law can badly misestimate the density. Strong-interaction phases, relativistic matter, anisotropic or inhomogeneous collapse, shocks, angular momentum and finite EFT cutoff all matter. This check explains how a bounce can arise and which assumption produces it.

10.2 Global causal structure and observational implications

A trapped surface is defined through the signs of the null expansions. A classical singularity theorem requires causal, energy and global hypotheses. A finite matter density or a regular minimum in $a(t)$ cannot determine the null expansions and event horizon of a rotating exterior. To turn (21) into an astrophysical model, specify initial stellar data and constraints, obtain a regular interior, match across a surface or physical shell to an exterior, track energy and angular momentum including emission, and locate trapped and anti-trapped regions through null geodesics. The interior may describe an expanding patch causally inaccessible to exterior observers. A white-hole-like exterior requires different global matching and a predicted escape channel. Ringdown changes, delayed bursts, and echoes each require a propagation and emission model plus a data likelihood. Existing black-to-white-hole tunneling and Einstein–Cartan daughter-universe proposals supply comparison models with their own assumptions. A6 A7 R38 R39

The reported handedness imbalance in a JWST deep field enters the archive as an observational lead. Projected galaxy winding, the intrinsic rotation vector, and global cosmic vorticity require an inclination and selection model to connect. A credible anisotropy test predefines redshift bins and sky masks, handles image mirroring and algorithmic symmetry, uses sky coverage beyond one field, and includes a kinematic explanation from observer motion and sample selection. An ESFD daughter-universe model would predict an axis, amplitude, sign and redshift dependence before the data split. It must also fit CMB isotropy and directional observables. The observed field imbalance measures its sample. It cannot identify a global formation mechanism without this

model. A7 R36 R40

11 Quark and gluon spin, the Higgs field, and CERN

11.1 Quark spin and the heavy-ion proposal

In the June 2 project discussion Grenke explicitly asked that intrinsic quark spin be part of the master theory. The archived terms are a quark tensor dipole and a gradient correction, $\alpha_q S^q_{\mu\nu} F^{\mu\nu} - \beta_q (\nabla_\rho S^q_{\mu\nu})^2$, with $S^q_{\mu\nu} = \bar{q}\sigma_{\mu\nu}q$ in that version. This normalization differs by two from the June Dirac $S_{\mu\nu}$. The term must be embedded with covariant derivatives and color and electroweak contractions when required. In a proton the total spin decomposition involves quark helicity, orbital angular momentum and gluon contributions, with operator definitions and a scale. In the Ji decomposition $J_q = \frac{1}{2}\Delta\Sigma_q + L_q$ and $J_q + J_g = \frac{1}{2}$, with a sum on flavors. Tensor charges relate transversity to the forward tensor bilinear. They are distinct from axial charges and the moments controlling magnetic couplings. Connecting the proposed operator to nucleon and neutron-star matter needs scale evolution and matched tensor matrix elements in the relevant composition and density. A1 A6 R03 R17

Peripheral high-energy nuclear collisions have orbital angular momentum, electromagnetic fields and short-lived vorticity. A fluid proxy for rotation seen by spin is thermal vorticity $\varpi_{\mu\nu} = -\frac{1}{2}(\partial_\mu \beta_\nu - \partial_\nu \beta_\mu)$ with $\beta_\mu = u_\mu / T$. Hyperon polarization inferred from weak decays and vector-meson spin alignment supply distinct observables. STAR measured global Λ polarization consistent with vortical dynamics, and an isobar blind analysis found no positive chiral magnetic signal under its predefined criterion. Charge-dependent backgrounds and isobar modeling enter the latter study. An ESFD term needs prediction of an additional dependence on flavor, p_T, rapidity, centrality, beam energy and spectator plane, with ordinary strong spin transfer and detector systematics. Compare isobars, matched centralities, and sign reversals only where the physical reaction-plane convention supplies a specified prediction. R04 R18 R30

The old claim of a 10^{-24} s electromagnetic microburst is a proposed formation timescale, an energy scale of $\hbar/\Delta t \simeq 0.66$ GeV. The 10^{-18} s instrumentation mentioned in the same draft is a million times coarser than that timescale. The suggested 10^6–10^7 photons per event in a 1–10 GeV band face a strict collision energy check. A 200 GeV-per-nucleon-pair Au–Au event has at most about 3.94×10^4 GeV of total center-of-mass beam energy before subtracting spectators and ordinary production. A 5.02 TeV Pb–Pb collision has about 1.04×10^6 GeV at the full-incoming-nuclei level. A million photons at 1 GeV already cost 10^6 GeV. The literal yield range therefore cannot describe a routine emitted component of these events. A feasible search uses direct-photon and low-mass dilepton spectra, angular anisotropies, photon correlations or polarization if measured, and comparisons with pp baselines and validated cocktail and thermal contributions. The coefficient should be matched to an emission rate and integrated over the spacetime history of each modeled event, including $\mathbf{B}(t)$ rather than an instantaneous upper estimate. A1 A6 R41

11.2 Higgs and the possibility of a common origin of mass and gravity

The established Higgs field is an electroweak scalar. Its vacuum value gives the weak vector masses and fermion masses through their respective couplings. The physical Higgs has spin zero. Most rest mass of nucleons emerges from the QCD state, including quark and gluon energies and

trace-anomaly physics, with the decomposition depending on scheme and scale. Energy of bound states is a source in GR regardless of how each constituent mass arose. The older ESFD proposal that Higgs, spin, gravity and electromagnetism descend from a common structure needs explicit matching to these distinct established processes. The invariant Φ in (3) is a proposed collective field or composite operator. It would mix with a Higgs-like scalar only through declared gauge-invariant terms and a specified vacuum. A4 A5 A6 R17 R42

Permissible comparison operators include $\Phi H^\dagger H$ with an appropriately dimensioned coefficient for a dimensionless Φ, nonminimal curvature $H^\dagger H R$, or the dimension-six electromagnetic matching contribution $(H^\dagger H)B^Y_{\mu\nu}B_Y^{\mu\nu}/M^2$ and weak-field analogues. After breaking, the last operator affects the gauge normalization and physical Higgs–gauge vertices in correlated ways. The long-range gravitational limit, observed $\gamma\gamma$, ZZ and WW channels, fifth-force limits, and electroweak precision data would jointly constrain such a model. The observed Higgs decay is a control measurement of the available couplings and correlated final states. It does not set the ESFD timing scale. R03 R42 R43

11.3 The off-shell density matrix and an ESFD residual

The September CERN expansion proposed $d\rho(q^2) = \rho_{\text{ESFD}}(q^2) - \rho_{\text{SM}}(q^2)$ in Higgs decays to four leptons, with q^2 the lower dilepton invariant mass squared under a fixed pairing. Timelike lepton currents in $H \to ZZ^{(*)} \to 4\ell$ encode the spin correlations of the vector channel. The second vector is generally off shell because $m_H < 2m_Z$. For a quantitative prediction start with the observable four-lepton amplitude, including identical-particle interference and gauge-complete contact and mixed $Z\gamma$ terms where applicable. Let q_1, q_2 be the dilepton momenta, D_Z the propagator factor, and $J^{(i)}$ the chiral lepton current. A schematic neutral-vector vertex description is

$$\begin{aligned}\mathcal{M}_{ZZ} \propto J^{(1)}_\mu J^{(2)}_\nu D_Z(q_1^2) D_Z(q_2^2)\big[a_1 m_Z^2 g^{\mu\nu} + a_2(q_1\cdot q_2\, g^{\mu\nu} - q_2^\mu q_1^\nu) \\ + a_3 \epsilon^{\mu\nu\rho\sigma} q_{1\rho} q_{2\sigma}\big].\end{aligned} \tag{22}$$

The tensor structures give spin and CP tests in a specified basis, with coefficients and form factors constrained by gauge symmetry and matching. For amplitudes $\mathcal{M}_\lambda$ projected to such a basis, $R_{\lambda\lambda'} = \int \mathcal{M}_\lambda \mathcal{M}^*_{\lambda'} d\Pi$ in a bin and $\rho = R/\operatorname{tr} R$. At first order, $\delta\rho = (\delta R - \rho_{\text{SM}} \operatorname{tr}\delta R)/\operatorname{tr} R_{\text{SM}}$, where δR includes interference. This enforces the trace constraint. Test physical positivity, fit the particular direction in angular coefficient space predicted by the operator, and background-subtract and fold detector acceptance with the same binning. A renormalized electroweak amplitude, joint covariance, and a detector model are necessary for a bound on the new coefficient. A5 R03 R44 R45

ATLAS's two published combined angular coefficients give observed minus Standard Model values $+0.26 \pm 0.45$ and -0.56 ± 0.44 using the quoted experimental marginal errors. The resulting marginal pulls are $+0.58$ and -1.27. They share analysis inputs and have no demonstrated joint ESFD likelihood in the recovered work. The 4.7σ ATLAS result concerns the assumed separable-state comparison in the angular analysis. CMS reports an I_3 95% interval [2.52, 2.75] in a restricted $C_\parallel$ fit and [0.28, 2.87] with both parameters profiled, with the Standard Model central reference 2.60. Event reconstruction and fit assumptions affect these comparisons. The study of top-quark spin entanglement is another Standard Model laboratory for density-matrix validation. It probes a different final state and interactions. A5 R44 R45 R46

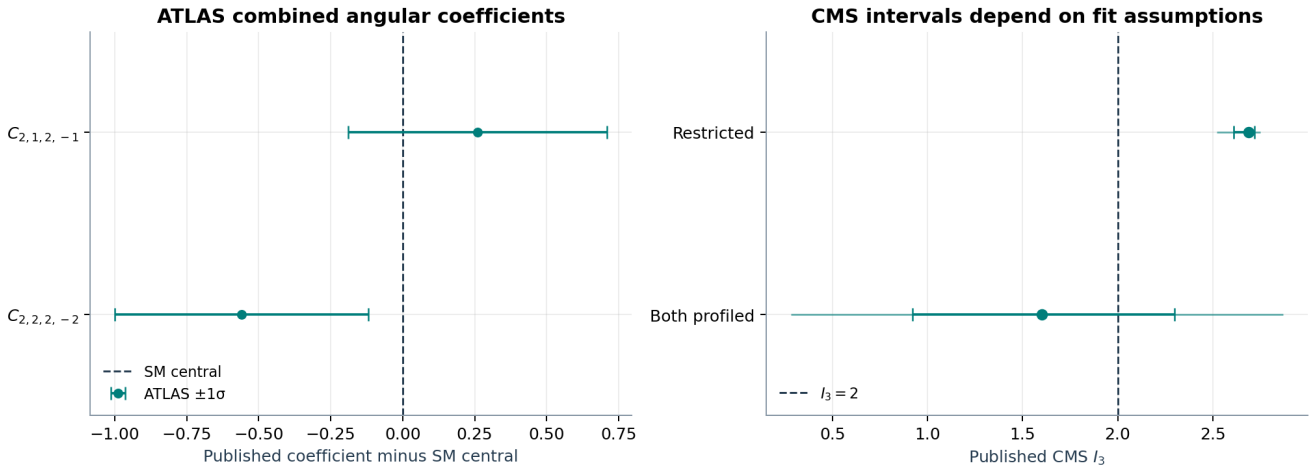


Figure 13. Published measurements used in the ESFD collider residual study. ATLAS points are relative to the reported Standard Model expectations. CMS intervals illustrate how the fit choice affects the witness. The figure contains measured values and Standard Model comparisons. A matched ESFD curve requires the amplitude in (22) to be specified.

12 Exceptional symmetry and ultraviolet completion

The archival July paper sketches $E_8 \supset \mathrm{Spin}(11,3) \to \mathrm{Spin}(3,1) \times H$ and an eventual low-energy Standard Model plus gravity. The frame-Higgs sector would connect a tetrad with a symmetry-breaking field. Heavy off-diagonal modes were proposed as a source of extra fermion, field, and torsion operators, with possible axion-like or heavy electroweak boson signatures. The proposal needs the real form, embedding of hypercharge, representations, chirality and generations, spectrum and vacuum, kinetic signs, symmetry breaking and anomaly checks. A positive identification of a gauge group supplies no Wilson coefficient without this chain. A6 R47

The E_8 root system has 112 vectors $\pm e_i \pm e_j$ for $i < j$ in $\mathbb{R}^8$, and 128 half-integer vectors $\frac{1}{2}(\pm 1, \ldots, \pm 1)$ with an even number of minus signs. Eight Cartan generators give dimension 248. In the compact real algebra or its complexification, the $\mathfrak{so}(16)$ branching reads $\mathbf{248} = \mathbf{120} \oplus \mathbf{128}$. The **120** is the adjoint, and the **128** is one chiral spinor of $\mathfrak{so}(16)$. This elementary representation check does not fix the noncompact embedding or supply four-dimensional chiral matter. Distler and Garibaldi identify representation-theoretic obstructions in the class of direct real/complex E_8 embeddings of gravity and the Standard Model that includes Lisi's proposal. An ESFD construction in the same class faces those assumptions. Higher-dimensional compactification, different algebraic structure, or different representations would have to be specified explicitly for a different proposal. R47

The old estimate $\chi \sim g_{E8}^2/M_X^2$ has mass dimension -2. Integrating out a healthy heavy vector with linear coupling to a fermion current can give a dimension-six current–current term $-g_X^2 J_X^2/(2M_X^2)$ at tree level in the stated vector convention. The low-energy spin–photon dipole of (1) has coefficient dimension -1. Its electroweak-gauge-invariant predecessor is a different dimension-six operator. Depending on the mediating fields, a dipole may first arise at loop level with Yukawa or fermion-mass insertions, or may require additional interactions. The minimal deliverable for this branch is a chiral table, charge and anomaly equations, canonical kinetic terms, an integration-out

calculation, and comparison of a single set of coefficients against multiparticle data. E_8 geometry, exceptional spinors, and analogies with the atomic wave hierarchy are motivations for this calculation. A6 R03 R47

13 Quantum coherence, collapse, and observers

13.1 Entanglement and a constrained spin-decoherence model

The older ESFD "shared envelope" gives spin correlations a common field description. Standard quantum states already permit nonfactorizing spin expectation values at spacelike separation. For a spin singlet $E(\mathbf{a},\mathbf{b}) = -\mathbf{a}\cdot\mathbf{b}$ and the optimal CHSH value is $2\sqrt{2}$. A locally causal model with independent settings and outcomes represented by $A_i(\lambda), B_j(\lambda) \in \{-1,+1\}$ has $|S| \leq 2$. For each hidden variable λ, either B_0+B_1 or B_0-B_1 is zero, so $A_0(B_0+B_1)+A_1(B_0-B_1)$ is ± 2. A shared pre-existing classical spin field and signals restricted to a future light cone still obey this bound under those assumptions. A change imposed at event A reaches only its causal future. Quantum field entanglement, a modified statistical assumption, or explicit nonlocal dynamics with operational no-signalling is needed if the model aims to reproduce the Bell correlations. An entanglement witness extracted from collider distributions has different operational assumptions than a freely chosen, spacelike separated Bell test. A1 A5 R48

A concrete test target for a local spin-sensitive environment is an additional positive dephasing rate $\Gamma(B,\Omega,\mathbf{M})$ above measured noise, with a completely positive Markovian model

$$\frac{d\rho}{dt} = -\frac{i}{\hbar}[H,\rho] + \Gamma(\sigma_z\rho\sigma_z - \rho). \tag{23}$$

The off-diagonal term decays as $e^{-2\Gamma t}$ in the commuting Hamiltonian frame. With independent such channels on the two qubits of $|\Phi^+\rangle$, the coherence multiplier is $\lambda = e^{-2\int(\Gamma_A+\Gamma_B)dt}$, and the maximal CHSH value is $2\sqrt{1+\lambda^2}$. Local completely positive trace-preserving operations preserve the distant marginal for unconditioned outcomes. A proposal coupling this rate to ESFD needs a dimensioned power law and control for magnetic gradients, control pulse noise, bath fluctuations and drift. For an objective-collapse hypothesis, the unconditioned dephasing equation gives an observationally different question from an account of individual outcomes. To go beyond ordinary dephasing, state the stochastic evolution of a run, probability rule, Lorentz/no-signalling limit and any heating or spontaneous radiation. Then use independent interferometry, entanglement visibility or timing constraints to infer a bounded rate. R48 R49

13.2 Time, observer layers, and consciousness

The Trap of Reality proposes that perception and spacetime are stabilized layers, that fields and spin may connect to an underlying observer, and that the nervous system may act as an interface or transducer. The public companion discussion also asks whether individual perspectives, continuity, and the origin of experience admit a broader field account. The analogy to Hoffman's Markovian conscious agents supplies a formal vocabulary for perception, decisions and actions. Tom Bilyeu's identity and continuity discussion supplies a philosophical comparison in the source. The ESFD field action as recovered models A, ψ, Φ and geometry. A consciousness or observer theory needs a defined variable, dynamics and independent observations linking it to these fields.

Connection by analogy, or the existence of spin coherence somewhere in matter, leaves that interface unspecified. A7 R50

For an operational model, assign an observer state o a state space $\mathcal{O}$, a generator $\mathcal{K}_o[\rho, \Phi, u]$, a readout $P(y|o, \rho, \Phi)$ for declared observables, and a reciprocal or explicitly open-system effect on matter. Fix units, a stress or energy account for any physical backreaction, and null limits. This would allow a preregistered laboratory comparison using the same instrument and environment with automated, blinded, and recorded conditions. Standard brain electrophysiology and signal artifacts are controls for a physical field claim. Subjective time and memory need independent definitions from proper time and population coherence. Philosophical claims about identity, free will, death, simulation, or consciousness in AI remain underdetermined by photon, pulsar and collider data. The archived views are retained as questions and can acquire empirical content through a specified discriminator. A7 R49 R50

14 Solar, geophysical, and vacuum extensions

14.1 Solar activity, local shear, and Earth

The rebuilt solar baseline uses the science-quality GOES composite flare measurements and WDC–SILSO daily counts. Removing invalid rows and repeats leaves 82,229 unique valid catalog entries. The monthly intersection has 81,721 flares across 381 complete months from February 1995 through October 2026, including 6,057 M/X flares and 366 X-class flares. A daily-exposure Poisson count baseline uses contemporaneous log-transformed activity, with 299 months before 2020 for the fit and 82 later months for evaluation. Its out-of-time mean Poisson deviance is 12.80 versus 41.71 for a constant-rate model. The all-period Spearman correlation of monthly M/X daily rate with sunspots is 0.863. Dependence within a solar cycle and concurrent activity preclude treating this as an advance warning forecast. The analysis is a calibrated solar-activity control for a later field-threshold model. R51

A generous 10 kG field and the Sun's representative bulk sidereal spin give $\chi_{\text{tim}} \simeq 4.56 \times 10^{-17}$. A model of active-region instability needs local vorticity, field projection and volume, photospheric flux emergence, helicity injection, preflare topology and reconnection physics. Start with a GOES event-to-active-region match, HMI vector magnetograms, and velocity estimates at uniform cadence. Approximately 37,247 solar entries in the full-month joined sample have a region identifier. The rest require an explicit missing-data model or a declared matched-cohort bound. A forecast should fit pre-event time only, and validate by active region and solar cycle, with disk position, sensitivity, false-alarm rate and retries of repeated flares handled consistently. A local plasma model compares magnetohydrodynamic current sheets, shearing and helicity thresholds with the spin closure; Earth's atmospheric response is another system with its own propagation and lags. A6 R51 R52

The older Earth-reset and tectonic proposals can be stated as a time-dependent field or torque claim. At an assumed geomagnetic field of 50 μT the magnetic pressure is about 1.0×10^{-3} Pa. A 100 nT perturbation gives a cross-stress scale $B\delta B/\mu_0 \simeq 4\times10^{-6}$ Pa. Geomagnetic reversals involve the dynamo field and require their own paleomagnetic chronology. They do not imply reversal of the planet's mechanical angular momentum. A missing high-gain triggering mechanism would require an energy pathway, independently observed electric currents or stresses at depth, and a lag, location and magnitude prediction scored on held-out catalogs. USGS reports no established

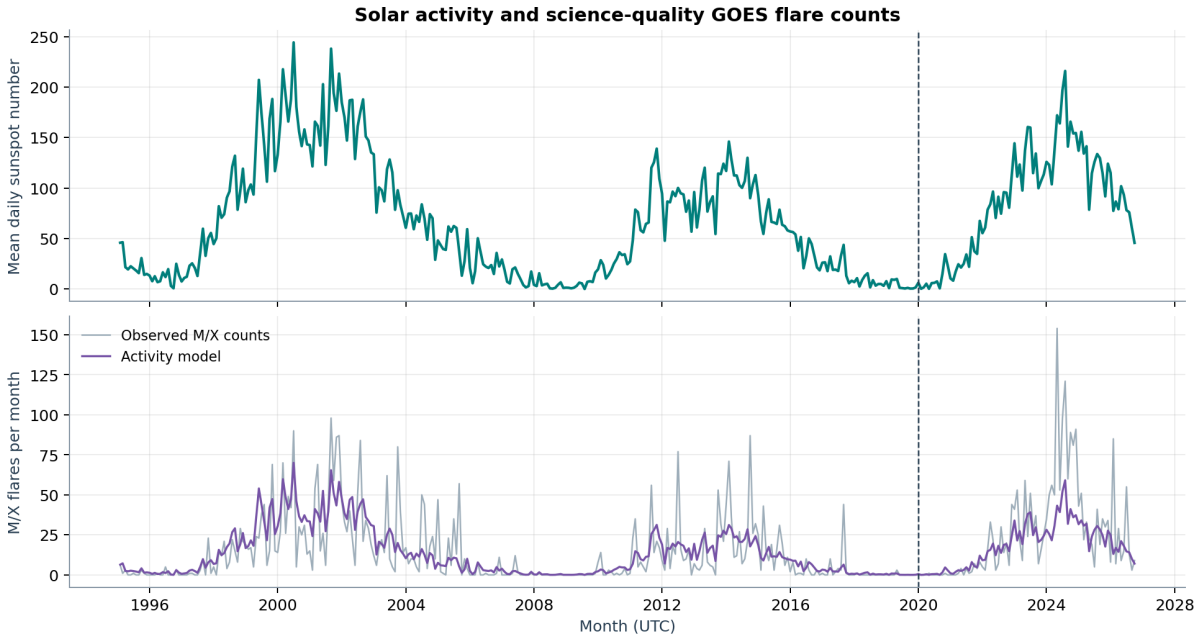


Figure 14. Solar baseline rerun on GOES and SILSO data. The dotted split marks the later monthly evaluation. The activity model uses contemporaneous sunspot measurements. Local spin and magnetic-field geometry remain an active-region-level test.

causal link between solar flares or magnetic storms and earthquakes. Independently demonstrate any such statistical relation against time clustering, catalog completeness, seismic seasonality and multiple searches. Earth-rotation and atmospheric angular-momentum exchange respond to geophysical and fluid forcing. They provide controlled alternative predictions. A6 R52 R53

14.2 Vacuum energy, claimed propulsion, and resonance traditions

The research archive links the early proposed spin torque and “vacuum resistance” to later work on Casimir physics, government research programs, and anomalous observations. The static Casimir energy of ideal parallel plates depends on separation, with $E/A = -\pi^2\hbar c/(720d^3)$ before material and geometry corrections. A closed reversible change of boundary configuration returns that energy difference during reset. The dynamical Casimir experiment generated photons under externally modulated boundaries, with the modulation supplying energy. These results are strong examples of field dynamics under boundary changes. An energy claim requires sustained power delivered under load and a full input, storage and environmental balance across the cycle. Open-circuit voltage alone can persist with very little transferable energy. A8 R54

The related Pattern Nexus work names NASA exploratory efforts, the DARPA vacuum-engineering program, a 2026 proposer slide reporting 100–250 mV at very low current density, a Casimir power-cell patent, and inertial reduction claims in the Pais patent record. These are traceable documents of research proposals, legal claims or reported bench observations. The physically decisive data for a putative vacuum source are long-duration $V(I,t)$ curves, integrated load energy, independent replication, and changes upon control stacks, chemical history, thermal gradients, ambient RF and leakage changes. Likewise for anomalous propulsion one compares the measured force with net momentum flux through the closed system, using calibrated thermal, outgassing, radiated power, cable and magnetic force budgets. A photon beam carrying power P emits mo-

mentum per time P/c in its direction. A closed internal electromagnetic cycle exchanges momentum within its components. A nonzero net thrust needs momentum carried across a boundary or a specified additional coupled field that carries it. The precise EMDrive remeasurement found that conventional thermal and apparatus effects can generate false positives. None of these documents calibrates an ESFD propulsion coefficient. A8 R54 R55 R56

The historical resonance discussion invokes ancient structures, Schumann modes, Tesla, Russell and Schauberger, and rotating or charged structures. The Great Pyramid electromagnetic simulation studied driven scattering and field concentration given specific material and geometry assumptions. For any finite passive resonator, $dU/dt = P_{\text{in}} - P_{\text{out}} - P_{\text{diss}}$ in the chosen convention. At 7.8 Hz, the approximate fundamental Schumann frequency, the free-space wavelength is about 3.84×10^7 m. A 200 m air-filled half-wave path instead has a simple scale of 7.5×10^5 Hz. Real dielectrics, losses and cavities change that scale, and coincidence with a global Earth–ionosphere oscillation requires actual coupling and loaded power measurements. Qualitative precedents of vortices, spirals, cavity modes or luminous discharges supply test geometries. Evidence of a historical energy device needs archaeological or physical records and a working electromagnetic power budget. A6 R57

The archived UAP and metric-engineering discussion maps reported accelerations or missing exhaust signatures to candidate physics. Calibrated range and velocity, platform motion, time-correlated independent sensors, energy and momentum accounting, and a known instrument transfer function are the data that would allow such an inference. An unresolved report supplies no quantitative ESFD coupling. A spacetime engineering claim is more demanding still, requiring a metric, a physical $T_{\mu\nu}$ and boundary data consistent with the source and causality. Public exploratory reports and intellectual overlaps support a history-of-ideas entry. The stronger claims about classified technology or deliberate suppression require independent evidence. A8 R56

15 Validation plan and decision criteria

The research question to carry forward is whether measured spin or spin correlations cause a residual that survives known electromagnetic, nuclear, gravitational and instrumental effects. The most constrained formulation starts with one operator or response law, one physical system, and one predeclared observable. A cross-scale model must produce several observables from shared coefficients and observable scale-matching functions. The tests below use that requirement to assign actual risk to competing branches.

15.1 Experiment and analysis specifications

Claim or observable	Matched control and data	Decision criterion
Extra local magnetic dipole	Species, charge and state matched against QED and hadronic moments, with independent fine-structure or lattice inputs.	Fit a signed new coefficient in a declared scheme. A replicated residual with correct operator dependence is needed. Limits are conditional on the operator basis.
Scalar mode onset (9)–(12)	Canonical scalar/photon, fixed magnetic topology, calibrated dimensions, independent f_Φ, m_0 or ξ if accessible.	Lower eigenvalue crosses zero in the predicted mode, angular or gap scaling, and finite-domain threshold. Require the same coefficient in propagation and onset.
Rotation, chirality, clock or inertia	Reversal factorial, matched inertial mass and spin composition, clock sensitivities or torque null channels.	A reproducible prespecified parity contrast and its amplitude bound, after measured environmental regressors.
Spin coherence or state reduction	Bell/Ramsey sequence with field/exposure windows and process noise calibrated.	Rate and basis dependence agree with the specified dynamical map. Compare to noise and use raw outcomes to check marginals.
Pulsar–magnetar threshold	Timing, independent field proxy, exposure and event-era data, source-disjoint validation.	Calibrated out-of-sample incremental likelihood above age, dipole and activity. Hard legacy class split already fails fixed counts.
Flares and glitches	Superfluid, torque and magnetoelastic timing, calibrated event exposures and contemporaneous field geometry.	Separate likelihoods per event family and a measurable dependence on the declared instability variable.
Magnetar polarimetry	QED, atmosphere, plasma and instrument transfer at the same phase and energy.	Joint Stokes likelihood for a single predicted residual over multiple sources or epochs.
New compact remnant stress	Shared GR and ESFD EOS, mass, angular momentum and topology, plus convergence-tested 3+1 data.	Stable, resolvable shift in equilibrium, oscillation, collapse or waveform mapped to a separately estimated field and spin.

Claim or observable	Matched control and data	Decision criterion
Compact-merger precursor	Arrival correction, independent detectors, live time, response matrices and matched off-source windows.	Population fluence/incidence or polarization bound with trials included and injection recovery. Positive candidate requires timed, replicated signal.
Galactic excess gravity	SPARC and new disjoint magnetic maps with baryons, stars, and lensing samples.	Same normalization predicts $V(r)$ and gravitational slip/lensing on disjoint galaxies. Fixed per-galaxy scale fitting supplies a shape comparison.
Cluster, CMB or cosmic structure	Joint lensing and baryon templates, BAO, CMB TT/TE/EE and growth, common selection support.	A consistent perturbation cosmology fits background, structure and lensing over redshift with shared parameters.
QGP or CERN residual	Standard Model amplitude/transport, background, detector full response and correlated fitting.	Operator-specific spectrum or angular direction, tested at fixed pairing and cuts in independent or withheld data.
Spin–torsion bounce	Covariant connection variation, microphysical equation of state, realistic shear and global geometry.	A stable bounce below computed validity scales and a predeclared external or cosmological observable.
Earth, vacuum devices, or field-observer	Matched environmental, energy and momentum channels, independent measurement and replicable protocol.	A predictive, dimensioned effect above the relevant baseline. Without a physical map the archive supplies a conjecture or proposal.

15.2 Statistical and numerical standards

Define the scientific unit before fitting. Repeated radii within a galaxy and repeated flares within an active region are correlated. Resample at the galaxy, source, or interval-block level as appropriate. A positive comparison against a flat null tests explanatory variation. To test an incremental spin mechanism, use a state-of-the-art baseline plus the measured spin predictor with equivalent access to inputs. For detection-like data, retain upper limits, exposure and selection efficiency. A measured effective field with geometry uncertainty is a latent-variable likelihood. For model comparison report pointwise residuals, a held-out score with uncertainty, and sensitivity to likelihood and priors. Any empirical choice of optimum threshold is trained in a development-only split, and legacy signed predictions remain frozen as archival controls.

An observational forward model is $\mathbf{y} = \mathcal{R}[\mathbf{h}_{\text{baseline}}(\boldsymbol{\eta}) + c_{\text{ESFD}}\,\mathbf{h}_{\text{spin}}(\boldsymbol{\theta})] + \boldsymbol{\epsilon}$ where $\mathcal{R}$ is the telescope, detector, or lab response and $\boldsymbol{\eta}$ holds nuisance parameters. Document the physical meaning, units, sign, and domain of validity of c_{ESFD} and $\boldsymbol{\theta}$. When available, quantify identifiability with the covariance-weighted derivative of the expected data after nuisance projection. If the predicted residual lies in the same direction as an age or calibration change, collect independent information that changes that degeneracy before interpreting a fitted coefficient. For a search across masses, bands, time windows or coefficients, estimate the global false-alarm probability using the same selection and entire search on the control set. Report a tested range for a null result, with sensitivity to injection and population assumptions.

For field computations validate conserved quantities and constraints, eigenvalue benchmarks, background recovery, units and numerical convergence. Vary mesh, time step, domain and dissipation settings. Record equations and their regularization, commits, compiler or Python versions, initial and boundary conditions, numerical cutoffs, and the parameter grid. Prespecify stability and nonlinear diagnostics. Qualitative agreement of an image or plot can be tested through its corresponding quantitative observable. A higher-order EFT term can sometimes be used perturbatively despite unphysical solutions of a fully resummed truncated equation. State explicitly which equations are solved and where their cutoffs lie.

15.3 What this edition establishes

The full rebuilt catalog pipeline and its summaries reproduce from the archived input snapshots. The longest-lived number in the original argument, Λ_{tim}, is useful as a historical comparison line, and with timing-inferred dipoles it carries exactly the information of a characteristic-age threshold. The class and recurrence tests do not support the hard cut. The new exponential-action analysis provides a separate result in a fully specified local problem. An exponential gauge coupling with a quadratic independent scalar can destabilize a transverse electromagnetic mode even when its prescribed-B scalar curvature is positive. The unstable band and rate are mathematical predictions under the stated action and boundaries. The matched vacuum birefringence gives a conditional lower bound of $2.67times10^{15}$ G on its onset. A prescribed spin source and a photon gap alter the threshold in distinct ways, giving quantitative targets for a real spin-polarized plasma model.

The galaxy exercises give a one-profile fit, held-out evaluations, absolute energy checks and a covariant target for a later joint fit. The spin hierarchy calculation shows why huge total particle counts, substantial mechanical angular momentum, and coherent microscopic spin need different inputs. The bounce calculation makes exact the conditions under which a negative stiff term produces a turnaround. Its extrapolation to a black-hole spacetime needs independent validation. The high-risk branches remain documented so a subsequent version can test their predictions and update the evidence.

16 Appendix A. Reconstruction ledger

The file **branch_register.csv** contains the more granular evidence and inference ledger. The table here identifies the version families and places their claims within this paper.

Version family and date evidence	Reconstructed content and disposition
June 2–3, 2025 project discussions and June Word version	Intrinsic spin, quark tensor, rigid rotors, the $B\Omega$ rule, saturation potential, clocks, QGP, solar or stellar flares, and merger precursor. Equations (1)–(2) and (13)–(15).
June 3 covariant synthesis in chat, later 2026 recap	Equation (3), historical ambiguity of independent versus composite Φ, time-feedback law, and torsion proposal. This edition restores the action from an excerpt and gives separate consistent variations, (4)–(7).
June consolidated SEFD, Electromagnetic Universe and quantum rewrite	Spin entropy, effective divergences, space and dark-matter alternatives, Pauli coupling, entanglement. Equations (8), (16)–(19), (23), and EFT matching.
June–July E_8, non-Abelian and UV extensions	Frame-Higgs and threshold narrative, masses and dipoles, Spin$(11,3)$, anomalous symmetry breaking, contact versus dipole matching. Section Exceptional symmetry.
Three project PDF manuscripts and December proof copy	Population separation, global energies, compact limits, spin-generated gravity and inertia, relativity and simulations. Rebuilt data and several numerical corrections. Original analyses omitted by old exports are catalogued as unavailable inputs.
2026 Aharonov–Casher and spin reorientation discussion	Neutral-particle phase, response mapping, conventional quantum controls, proposed rotation/field reversal. Section Laboratory spin.
September 17, 2026 CERN versions	Higgs entanglement, off-shell vector density matrix, later distinction between ESFD residual and standard baseline. Equation (22), ATLAS and CMS comparisons.
Later observer and wave discussion, September 2026 cosmology	Observer interface, nested wave geometry, spin–torsion bounce and white-hole/daughter-universe scenarios. Equations (20)–(21), global matching and Bell/observer analysis.
Later related vacuum and astrophysical essays	Resonance, propulsion, anomalous observations, cosmic structure, Earth and vacuum questions. Environmental energy balance, field strength and evidence requirements.

Additional historical numerical claims discussed in the project records include oscillation and

glitch correlations in tiny hand-selected samples, predicted suppression scales near 100 MeV or 10–100 GeV depending on the draft, $\chi \lesssim 10^{-3}$ as an unspecified low-energy coefficient, and cosmic f_{NL} of order unity. A proposed value without operator definitions and a computed response remains an archival claim. In the re-evaluation PDF an external magnetosphere difference under 1%, a spin-fluid Poisson correction of order 10^{-8}, and a null spinning-ring or inertia test are described. The required equations, source parameters and run records are absent from the recovered inputs. They enter this edition as attributed statements. The new local stability solve, verified radius profiles, and TOV benchmarks provide independent calculations with defined assumptions. A1 A2 A6

17 Appendix B. Reproducible calculations and data dictionary

17.1 Included reruns

The companion ZIP places the data and prior pipeline directly in **baseline/**. It includes 28 hashed inputs, among them complete ATNF and McGill timing snapshots and a HEASARC mirror, SPARC profiles, GOES and SILSO series, six LALSuite EOS tables, GWOSC and later Zenodo PE summaries, Fermi TTE files, and transcriptions of selected ATLAS, CMS and IXPE results. The original 19-file recovery archive and its 40-lead inventory travel with the data. **input_manifest.csv** records URLs, members, checksums, and metadata when exposed upstream. Each catalog has independent update dates. The script checks all hashes and reconstructs the baseline summary and plot data before the master analyses. Definitions such as “confirmed,” “tagged,” “included event,” or “published interval” are tied to the relevant source.

Computation	Machine-readable outputs in the master package
Catalogs and historical cutoff	**baseline/results/atnf_catalog_with_metrics.csv**, **mcgill_catalog_with_metrics.csv**, **mcgill_alternate_timing_values.csv**, **glitch_recurrence_cohort.csv**.
TOV and mass/spin	**baseline/results/tov_sequences.csv**, **tov_maxima.csv**, **canonical_compact_energy_checks.csv**, **gwtc_cumulative_events.csv**, **gwtc_remnant_spin_summary.csv**.
Rotation and mass-scale checks	**baseline/results/sparc_all_radii.csv**, **sparc_model_fits.csv**, **sparc_model_predictions.csv**, **legacy_dwarf_and_cluster_scale_checks.csv**.

Computation	Machine-readable outputs in the master package
Transients, solar and collider	**baseline/results/gw170817_gbm_detectors.csv**, **gw170817_gbm_offset_scan.csv**, **gw170817_gbm_offsource_controls.csv**, **goes_silso_joined_months.csv**, **atlas_angular_residuals.csv**, **cms_polarization_witness_checks.csv**, **ixpe_polarization_benchmark.csv**.
Scalar growth and finite-size threshold	**results/esfd_scalar_stability.csv**, **esfd_scalar_dispersion.csv**, **esfd_scalar_evolution.csv**, **esfd_scalar_pvlas.csv**.
Spin alignment, flags and polarization	**results/esfd_timing_orientation.csv**, **esfd_spin_polarization.csv**, **esfd_spin_coarse_graining.csv**.
Gravitating magnetic field and torsion	**results/esfd_galaxy_magnetic_energy_budget.csv**, **esfd_torsion_bounce.csv**.

The scalar sweep uses $B/B_c = 0$ to 4 and angles 0° to 90°. Azimuth enters only through the stated background symmetry. The illustrative time integration includes an otherwise stable normal-mode admixture. Galaxy residual estimates use the largest eligible measured radius per matched fit and the square root of a volume-equivalent mass budget. The orientation calculation uses $0.5 \leq s_B \leq 4$ including exact rows at unity and two, and analytic probabilities under an assumed isotropic axis distribution. The degenerate gas model uses the neutron magnetic moment from the software constants and a density 0.16 fm^{-3}. The torsion toy sets $a/a_b = 1$ and $Ht_b = 0$ at the bounce. **baseline/results/summary.json** and **results/spin_benchmarks_summary.json** provide exact summary values. Reproduction commands, dependency versions and reference information accompany this document.

17.2 Cross-scale correspondence and invalidation

The data cover mostly one-variable or reduced-model consequences. To claim a common ESFD mechanism across scales, a parameter matched to a dipole measurement must give the same low-energy scattering result, and a spin susceptibility calibrated in a stated medium must predict the sign and magnitude of the response in the qualified domain. A claimed relation between susceptibility and spin-down damping needs competing torques and independent B, and a claim about curvature needs independent dynamics and lensing. Predefined uncertainty envelopes convert failures to operator bounds. When multiple independently normalized operators are allowed, tests constrain each measured response and the rank of the joint inference. These requirements prevent a new expression for χ from absorbing a failed prediction by changing its definition after the measurement.

18 Sources and references

18.1 ESFD project sources

A1 Grenke, Christopher. *Spin–Field Saturation Dynamics (ESFD): A Unified Framework for Emergent Gravity, Collapse, and Quantum Coherence*. June 3, 2025 Word metadata, archived as **6-3-spin ESFD current .docx**. Sections 3, 5, 8–11 and 14–17 supply the principal original equations, phenomenological cutoff, laboratory proposals and extensions.

A2 *Re-Evaluation of Electromagnetic Spin–Field Dynamics (ESFD) Theory*. Recovered 18-page project PDF. The text reports weak-coupling tests and a set of simulations. Section 3 is the historical record of those simulations.

A3 *Testing Electromagnetic Spin–Field Dynamics (ESFD) Theory with Astrophysical Data*. Recovered five-page project PDF. Sections 1–3 introduce the canonical energy comparison and pulsar, magnetar and compact-object reference values.

A4 *Proof of the Electromagnetic Spin–Field Dynamics (ESFD) Theory*. Recovered 22-page project PDF and editable counterpart, with the latter dated December 10, 2025 in its metadata. The proof title identifies the historical document. Sections 2–6 include the action sketch, emergent-gravity case and normalized saturation variables.

A5 Grenke, Christopher. 2026 September 17 CERN-era drafts, including **PN_ESFD_CERN_FULL_FRAMEWORK_CMS_BODY.html**, the original and corrected Higgs entanglement articles, and their entry/source records. ESFD project topic at Pattern Nexus.

A6 ESFD project conversation excerpts from June–September 2025, December 2025, and June–September 2026. The package's **provenance/historical_notes.md** identifies dates and speaker roles where recovered. The 2025 June 3 covariant-action excerpt and the later corrected-model recap are distinct from the available June Word file. The **recovery_leads.csv** record inside the original archive identifies unavailable original bytes and runs.

A7 Grenke, Christopher. *The Trap of Reality: Consciousness, the Observer, and the Field Layer Beneath Spacetime*. Three archived 2026 text versions and a later related Pattern Nexus consciousness preview. The wave-emergence discussion is dated December 2025. Published observer essay.

A8 Grenke, Christopher. *The Vacuum Program: Zero-Point Energy, UAP Disclosure, and the Physics Hiding in Plain Sight*. Related project working HTML and sources in **provenance/related/**, alongside the prior recovery register and research histories.

18.2 Physics literature and data

R01 Hehl, F. W., von der Heyde, P., Kerlick, G. D., and Nester, J. M. (1976). *General relativity with spin and torsion: Foundations and prospects*. Reviews of Modern Physics 48, 393. Shapiro, I. L. (2002). *Physical aspects of the space-time torsion*. Physics Reports 357, 113–213. Hehl et al. · Shapiro.

R02 Fan, X., Myers, T. G., Sukra, B. A. D., and Gabrielse, G. (2023). *Measurement of the electron magnetic moment*. Physical Review Letters 130, 071801. Schwinger, J. (1948). Leading radiative magnetic moment result. Fan et al. · Schwinger.

R03 Grzadkowski, B., Iskrzyński, M., Misiak, M., and Rosiek, J. (2010). *Dimension-six terms in the Standard Model Lagrangian*. JHEP 10, 085. Operator basis and conventions.

R04 Becattini, F., and Lisa, M. A. (2020). *Polarization and vorticity in the quark–gluon plasma*. Annual Review of Nuclear and Particle Science 70, 395–423. Review.

R05 Spitkovsky, A. (2006). *Time-dependent force-free pulsar magnetospheres: axisymmetric and oblique rotators*. Astrophysical Journal Letters 648, L51–L54. Paper.

R06 Adler, S. L. (1971). *Photon splitting and photon dispersion in a strong magnetic field.* Annals of Physics 67, 599–647. Dunne, G. V. (2004). *Heisenberg–Euler effective Lagrangians: basics and extensions*. Adler · Dunne.

R07 Aharonov, Y., and Casher, A. (1984). *Topological quantum effects for neutral particles*. Physical Review Letters 53, 319. Cimmino, A., et al. (1989). Neutron interferometry measurement. Sangster, K., et al. (1993). Atom interferometry measurement. Theory · Neutrons · Atoms.

R08 Manchester, R. N., Hobbs, G. B., Teoh, A., and Hobbs, M. (2005). *The Australia Telescope National Facility pulsar catalogue*. Astronomical Journal 129, 1993. Public 2.9.0 timing and glitch snapshots and HEASARC compilation. Olausen, S. A., and Kaspi, V. M. (2014). McGill magnetar catalog. ATNF paper · CSIRO catalog · HEASARC mirror · McGill paper · McGill tables.

R09 Kaspi, V. M., and Beloborodov, A. M. (2017). *Magnetars*. Annual Review of Astronomy and Astrophysics 55, 261–301. Review.

R10 Gavriil, F. P., et al. (2008). *Magnetar-like emission from the young pulsar in Kes 75*. Science 319, 1802–1805. NASA Fermi Crab Nebula flare summary. Kes 75 study · Crab Nebula observations.

R11 CHIME/FRB Collaboration (2020). *A bright millisecond-duration radio burst from a Galactic magnetar*. Nature 587, 54–58. Observation.

R12 Viganò, D., et al. (2013). *Unifying the observational diversity of isolated neutron stars via magneto-thermal evolution models*. Monthly Notices of the Royal Astronomical Society 434, 123–141. Magneto-thermal comparison.

R13 Israel, G. L., et al. (2005). *The discovery of rapid X-ray oscillations in the tail of the SGR 1806–20 hyperflare*. Astrophysical Journal Letters 628, L53. QPO study.

R14 Hessels, J. W. T., et al. (2006). *A radio pulsar spinning at 716 Hz*. Science 311, 1901–1904. Breu, C., and Rezzolla, L. (2016). *Maximum mass, moment of inertia and compactness of relativistic stars*. MNRAS 459, 646–656. 716 Hz observation · Uniform rotation estimates.

R15 Taverna, R., et al. (2022). *Polarized X-rays from a magnetar*. Science 378, 646–650. IXPE result.

R16 Tolman, R. C. (1939). Static relativistic fluid solutions. Oppenheimer, J. R., and Volkoff, G. M. (1939). Massive neutron core equilibrium. LALSuite public EOS tables, software release 8.0.2 in the snapshot. Tolman · Oppenheimer–Volkoff · LALSuite.

R17 Ji, X. (1997). *Gauge-invariant decomposition of nucleon spin.* Physical Review Letters 78, 610. Yang, Y.-B., et al. (2018). *Proton mass decomposition from the QCD energy momentum tensor*. Physical Review Letters 121, 212001. Ji · Yang et al..

R18 STAR Collaboration (2017). *Global Λ hyperon polarization in nuclear collisions*. Nature 548, 62–65. STAR Collaboration (2022). Blind analysis of the chiral magnetic effect in isobar collisions. Physical Review C 105, 014901. Polarization · Isobar analysis.

R19 Kerr, R. P. (1963). *Gravitational field of a spinning mass as an example of algebraically special metrics*. Physical Review Letters 11, 237. GWOSC cumulative event snapshot and GWTC-4.1/5.0 PE tables. LVK GW230529 event. Kerr · GWOSC · GWTC-4.1 PE · GWTC-5.0 PE · GW230529.

R20 Blandford, R. D., and Znajek, R. L. (1977). *Electromagnetic extraction of energy from Kerr black holes*. MNRAS 179, 433–456. Paper.

R21 LIGO, Virgo, Fermi GBM and INTEGRAL (2017). *Gravitational waves and gamma-rays from a binary neutron star merger: GW170817 and GRB 170817A*. ApJL 848, L13. Public Fermi GRB170817A time-tagged events. Joint analysis · GBM data.

R22 Xiao, S., et al. (2022). *The peculiar precursor of a gamma-ray burst from a binary merger involving a magnetar*. Precursor study and QPO candidate.

R23 Touboul, P., et al. (2022). *MICROSCOPE mission: final results of the test of the equivalence principle*. Physical Review Letters 129, 121102. Final result.

R24 Bothwell, T., et al. (2022). *Resolving the gravitational redshift across a millimetre-scale atomic sample*. Nature 602, 420–424. Clock measurement.

R25 Everitt, C. W. F., et al. (2011). *Gravity Probe B: final results of a space experiment to test general relativity*. Physical Review Letters 106, 221101. Frame-dragging measurement.

R26 Beck, R. (2016). *Magnetic fields in spiral galaxies*. Astronomy and Astrophysics Review 24, 4. Observational review.

R27 Heckel, B. R., et al. (2008). *Preferred-frame and CP-violation tests with polarized electrons*. Physical Review D 78, 092006. Polarized torsion pendulum.

R28 Lelli, F., McGaugh, S. S., and Schombert, J. M. (2016). *SPARC: mass models for 175 disk galaxies with Spitzer photometry and accurate rotation curves*. Astronomical Journal 152, 157. Paper · Data.

R29 McGaugh, S. S., Lelli, F., and Schombert, J. M. (2016). *Radial acceleration relation in rotationally supported galaxies*. Physical Review Letters 117, 201101. Reference relation.

R30 Fukushima, K., Kharzeev, D. E., and Warringa, H. J. (2008). *The chiral magnetic effect*. Physical Review D 78, 074033. Constitutive effect.

R31 Visser, M. (2002), review of Sakharov induced gravity. Jacobson, T. (1995), thermodynamic field-equation argument. Verlinde, E. (2011), entropic-gravity proposal. Visser · Jacobson · Verlinde.

R32 Haisch, B., Rueda, A., and Puthoff, H. E. (1994). *Inertia as a zero-point-field Lorentz force*. Physical Review A 49, 678. Cramer, J. G. (1986). *The transactional interpretation of quantum mechanics*. Reviews of Modern Physics 58, 647. Vacuum-inertia proposal · Transactional interpretation.

R33 Wolf, J., et al. (2010). Masses of dispersion-supported galaxies. Umetsu, K., et al. (2015). Weak-lensing analysis of Abell 1689. Draco half-light estimate · Abell 1689 comparison.

R34 Alves, J., et al. (2020). *A Galactic-scale gas wave in the solar neighbourhood*. Nature 578, 237–239. Konietzka, R., et al. (2024). *The Radcliffe Wave is oscillating*. Nature 628, 62–65. Tully, R. B., et al. (2014). *The Laniakea supercluster of galaxies*. Nature 513, 71–73. Radcliffe discovery · Wave kinematics · Peculiar velocity structure.

R35 Clowe, D., et al. (2006). Bullet Cluster weak-lensing and baryon offset. Astrophysical Journal Letters 648, L109–L113. Weak-lensing study.

R36 Planck Collaboration (2020). Planck 2018 cosmological parameters and primordial non-Gaussianity analyses. Parameter results · Non-Gaussianity constraints.

R37 Planck Collaboration (2016), primordial magnetic fields. Minami, Y., and Komatsu, E. (2020), cosmic polarization analysis. Magnetic field constraints · Birefringence methods.

R38 Popławski, N. J. (2010, 2016, 2020). Einstein–Cartan cosmology and spin-fluid collapse examples. Cosmology with torsion · Universe in a black hole · Collapse with torsion.

R39 Penrose, R. (1965), gravitational collapse and spacetime singularities. Haggard, H. M., and Rovelli, C. (2015), black-to-white hole tunneling proposal. LVK (2021), GR tests with GWTC-3. Singularity theorem · Tunneling proposal · Waveform tests.

R40 Shamir, L. (2025). *The distribution of galaxy rotation in JWST Advanced Deep Extragalactic Survey*. MNRAS 538, 76–91. Deep-field result.

R41 ALICE Collaboration (2016). *Direct photon production in Pb–Pb collisions at 2.76 TeV*. Physics Letters B 754, 235–248. Photon spectra.

R42 CERN. Higgs field and boson, physical context and discovery summary. Higgs overview.

R43 Bezrukov, F. L., and Shaposhnikov, M. (2008). *The Standard Model Higgs boson as the inflaton*. Physics Letters B 659, 703–706. Nonminimal-curvature model.

R44 ATLAS Collaboration (2026). *Measurements of Z-boson pair entanglement in decays of Higgs bosons at the ATLAS experiment*. Relevant angular coefficients are in Table 1. Paper with table · Result record.

R45 CMS Collaboration. *Study of spin correlations in Higgs boson decays to four leptons*. CMS-PAS-HIG-25-011. Results, figures and covariance context.

R46 ATLAS Collaboration (2024). *Observation of quantum entanglement with top quarks at the ATLAS detector*. Nature 633, 542–547. Top-quark result.

R47 Lisi, A. G. (2007). *An exceptionally simple theory of everything*. Distler, J., and Garibaldi, S. (2010). *There is no "theory of everything" inside E_8*. Communications in Mathematical Physics 298, 419–436. Lisi proposal · Distler–Garibaldi obstruction.

R48 Clauser, J. F., Horne, M. A., Shimony, A., and Holt, R. A. (1969), correlation inequality. Horodecki, R., Horodecki, P., and Horodecki, M. (1995), criterion for two-qubit CHSH violation. Hensen, B., et al. (2015), loophole-free spin test. CHSH · Two-qubit criterion · Spin experiment.

R49 Lindblad, G. (1976). *On the generators of quantum dynamical semigroups*. Communications in Mathematical Physics 48, 119–130. Bassi, A., et al. (2013). Collapse models and experimental tests. Reviews of Modern Physics 85, 471. Generator · Collapse models.

R50 Hoffman, D. D., and Prakash, C. (2014). *Objects of consciousness*. Frontiers in Psychology 5, 577. Conscious-agent proposal.

R51 NOAA National Centers for Environmental Information, GOES science-quality flare report. WDC–SILSO, Royal Observatory of Belgium, Brussels, daily sunspot numbers. The package contains project-provided snapshots of the two sources. GOES documentation · SILSO data.

R52 Bobra, M. G., et al. (2014). HMI vector magnetic field pipeline and Space-Weather HMI Active Region Patches. Solar Physics 289, 3549–3578. NOAA Space Weather Prediction Center. SHARP field data methods · Space weather reference.

R53 U.S. Geological Survey. Geomagnetic disturbances and earthquake science. USGS earthquake causation FAQ.

R54 Jaffe, R. L. (2005). *Casimir effect and the quantum vacuum*. Physical Review D 72, 021301. Wilson, C. M., et al. (2011). *Observation of the dynamical Casimir effect in a superconducting circuit*. Nature 479, 376–379. Static interpretation · Driven experiment.

R55 Tajmar, M., Neunzig, O., and Weikert, M. (2021). *High-accuracy thrust measurements of the EMDrive and elimination of false-positive effects*. Pais, S. C., U.S. Patent 10,144,532. Precision thrust study · Patent record.

R56 DARPA ARRIVE research description and 2026 ExPEDitions proposer lightning talks, including the reported power-cell voltages. NASA independent UAP report and public scientific FAQ. Related vacuum documentation in A8. ARRIVE · Proposer slides · NASA UAP scientific summary.

R57 Balezin, M., et al. (2018). *Electromagnetic properties of the Great Pyramid: first multipole resonances and energy concentration*. Journal of Applied Physics 124, 034903. Driven-scattering study.

R58 Wigner, E. P. (1939). *On unitary representations of the inhomogeneous Lorentz group*. Annals of Mathematics 40, 149–204. Particle spin representations.

R59 Event Horizon Telescope Collaboration (2019), first M87 shadow results. NANOGrav Collaboration (2023), 15-year stochastic-background evidence. EHT baseline · NANOGrav baseline.

R60 Ejlli, A., Della Valle, F., Gastaldi, U., Messineo, G., Pengo, R., Ruoso, G., and Zavattini, G. (2020). *The PVLAS experiment: a 25 year effort to measure vacuum magnetic birefringence*. Physics Reports 871, 1–74. Final measurement and convention.